Title: Coherent spin manipulation of individual atoms on a surface

Authors: Kai Yang,[1,*] William Paul,[1] Soo-Hyon Phark,[1,2,3] Philip Willke,[1,2,4] Yujeong Bae,[1,2,4] Taeyoung Choi,[2,3] Taner Esat,[1,2,4] Arzhang Ardavan,[5] Andreas J. Heinrich,[2,3,*] and Christopher P. Lutz[1,*]

Affiliations:

[1]IBM Almaden Research Center, San Jose, CA 95120, USA.

[2]Center for Quantum Nanoscience, Institute for Basic Science (IBS), Seoul 03760, Republic of Korea.

[3]Department of Physics, Ewha Womans University, Seoul 03760, Republic of Korea.

[4]Ewha Womans University, Seoul 03760, Republic of Korea.

[5]CAESR, Clarendon Laboratory, Department of Physics, University of Oxford, Oxford OX1 3PU, UK.

*Correspondence to: k.yang@ibm.com; heinrich.andreas@qns.science; cplutz@us.ibm.com

Abstract: Achieving time-domain control of quantum states with atomic-scale spatial resolution in nanostructures is a long-term goal in quantum nanoscience and spintronics. Here, we demonstrate coherent spin rotations of individual atoms on a surface at the nanosecond timescale, using an all-electric scheme in a scanning tunneling microscope (STM). By modulating the atomically-confined magnetic interaction between the STM tip and surface atoms, we drive quantum Rabi oscillations between spin-up and spin-down states in as little as ~20 nanoseconds. Ramsey fringes and spin echo signals allow us to understand and improve quantum coherence. We further demonstrate coherent operations on engineered atomic dimers. The coherent control of spins arranged with atomic precision provides a solid-state platform for quantum-state engineering and simulation of many-body systems.

One Sentence Summary: Quantum spin states of atoms individually positioned on a surface are coherently manipulated using a scanning tunneling microscope.

Main Text: Detecting and controlling the coherent dynamics of artificial spin systems with single-spin resolution could provide fundamental insight into quantum magnetism (*1, 2*). A key technique for realizing coherent control is pulsed spin resonance, which traditionally uses short bursts of oscillating magnetic fields to induce transitions between selected quantum spin states (*3*). Coherent

spin manipulation lies at the heart of spin-based quantum information processing and coherent spintronic devices (*4*). In the solid-state environment, coherent control of single spins has been performed on molecules in break junctions (*5*), quantum dots and dopants in semiconductors (*6, 7*), as well as nitrogen-vacancy centers in diamond (*8, 9*). It would be desirable to image and precisely modify the local environment and energy-level structures at the atomic scale.

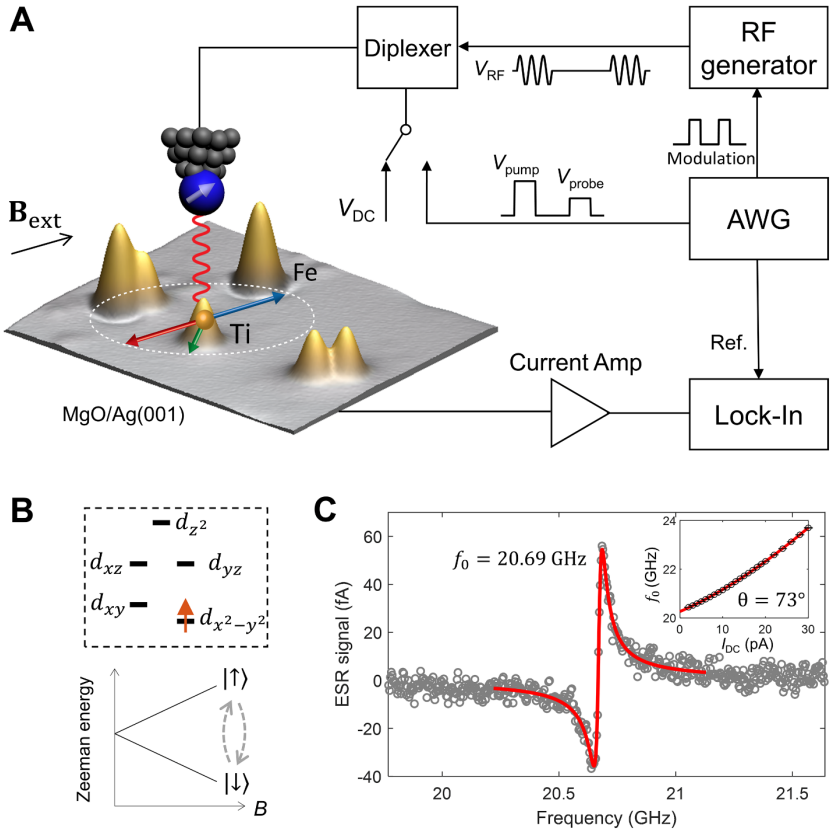

Fig. 1. **An STM circuit to manipulate spins of individual atoms**. (**A**) Schematic showing the low-temperature (T = 1.2 K) STM integrated with a radio-frequency (RF) generator and an arbitrary waveform generator (AWG), as well as an STM image (8.4 nm ×10 nm) of Ti and Fe atoms on a bilayer MgO on Ag(001) (setpoint: V_{DC} = 60 mV, I_{DC} = 10 pA). Exchange coupling (red wavy line) with the tip magnetic moment (white arrow) drives Ti spin resonance. The tip magnetoresistively senses the different Ti spin orientations, indicated by the red (|↓⟩ state), blue (|↑⟩ state) and green (superposition state) arrows. (**B**) Top: Orbital occupancy of the $3d^1$ configuration. Bottom: Zeeman energy of the Ti spin. (**C**) CW-ESR spectrum of a single Ti atom, fitted to an asymmetric Lorentzian (equation (S14)) (V_{DC} = 50 mV, I_{DC} = 5 pA, V_{RF} = 50 mV, B_{ext} = 0.82 T). Inset: resonant frequency f_0 as a function of I_{DC} at a constant V_{DC} = 50 mV. Fitting (red curve) to equation (S17) yields an angle θ = 73° between tip's magnetic moment and $\mathbf{B}_{ext}$.

Atomic-scale structures can be constructed and imaged with a scanning tunneling microscope (STM), which can probe spin-spin interactions (*10, 11*), spin dynamics (*12-14*) and

single-molecule motion (*15, 16*). Notably, artificial nanostructures built by STM have developed into a fruitful testing ground for exploring quantum magnetism (*11, 12, 14, 17-22*). Recently, continuous-wave (CW) electron spin resonance (ESR) was combined with spin-polarized STM to detect spin states with highly improved energy resolution (*22-24*).

The time evolution of a spin state can be accurately controlled by applying pulsed electromagnetic fields (*3*). In semiconductor heterostructures, coherent spin dynamics have been measured with STM by using femtosecond light pulses (*13*). Single-spin coherent control has not been achieved in STM because the spin manipulation time was long compared to the coherence time (*22*). Here, we demonstrate coherent spin manipulations at the single-atom scale, achieved by modulating the magnetic exchange interaction between the STM tip and the Ti atom on a surface using the time-varying electric field in the STM junction (Fig. 1A) (*25*).

The Ti atoms were separated from the Ag substrate with a bilayer MgO film, and were most likely hydrogenated (Supplementary Materials and Methods) (*24*). We referred to them simply as Ti. Each Ti atom has an electron spin $S = 1/2$, and was adsorbed either on top of a surface oxygen atom or at a bridge site between two oxygen atoms (*24, 26*). The two spin states $|\downarrow\rangle$ and $|\uparrow\rangle$, with electron spin quantum number $m_s = \pm 1/2$, were separated by the Zeeman energy in the presence of an applied magnetic field (Fig. 1B). In addition to the direct-current (DC) voltage V_{DC}, a radio-frequency (RF) voltage was applied with an amplitude V_{RF} at the STM tunnel junction (*22, 24*).

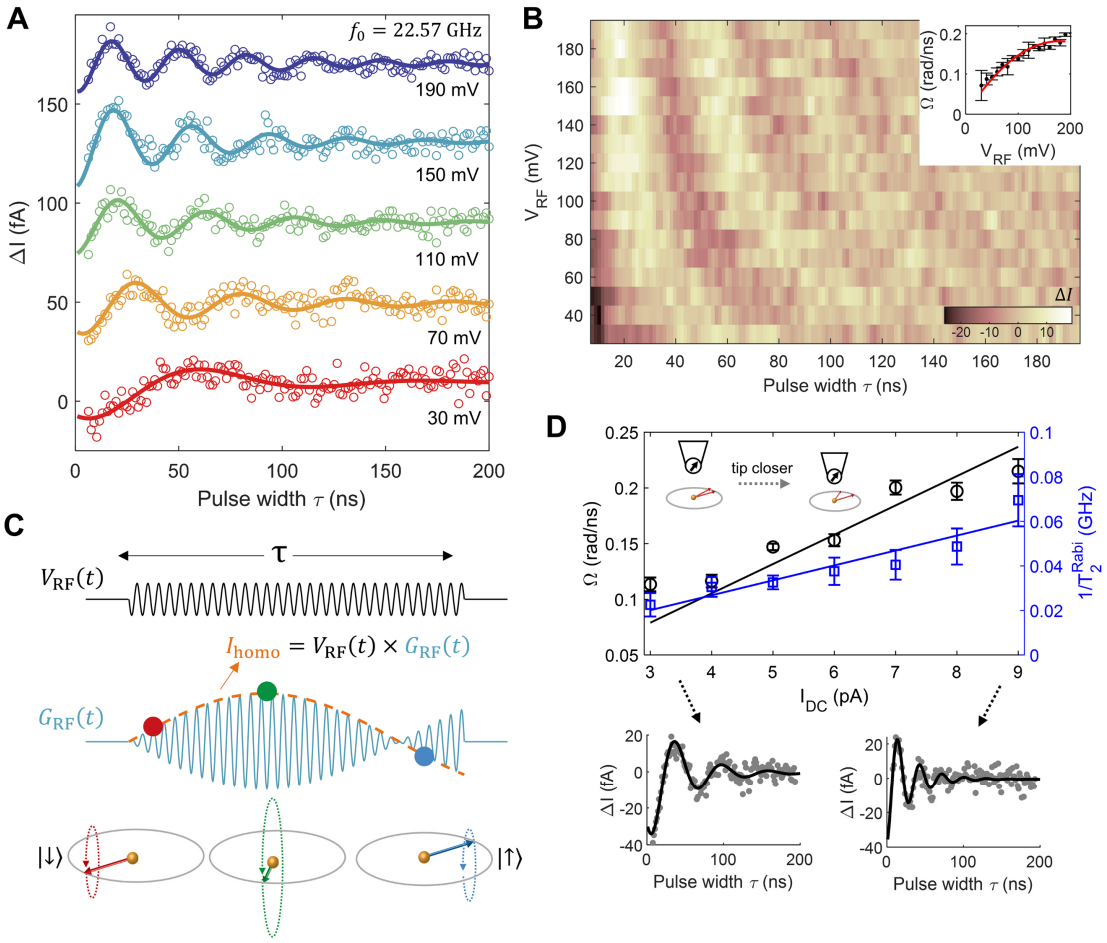

Fig. 2. Coherent control of a single Ti spin. (**A**) Rabi oscillations of a Ti spin at different V_{RF} as indicated (V_{DC} = 60 mV, I_{DC} = 4 pA, B_{ext} = 0.90 T). The RF frequency is on resonance at f_0 = 22.57 GHz (Fig. S6A). Solid curves are sinusoidal fits to the tunnel current signal ΔI. The data are offset vertically for better visibility. Each spectrum was measured for ~20 min. (**B**) Rabi oscillations represented in color scale shown, over a fine grid of τ and V_{RF}. Inset: **Ω** at different V_{RF} fitted to a quadratic polynomial with zero offset. (**C**) Schematics showing the homodyne detection of the Rabi oscillations by measuring current I_{homo}, the time-averaged product of G_{RF} and V_{RF}. G_{RF}(t) is the instantaneous tunnel conductance when V_{RF} (t) is on. Pulse width τ was controlled by the AWG. (**D**) **Ω** and $1/T_2^{Rabi}$ at different tip-atom distances set by different I_{DC} at V_{DC} = 50 mV (V_{RF} = 80 mV, B_{ext} = 0.82 T). Solid lines are linear fits. Lower panels show the Rabi oscillations with fitting at I_{DC} = 3 pA (left) and 9 pA (right).

The magnetic field experienced by a Ti spin (**S**) is the vector sum of the externally applied static field $\mathbf{B}_{ext}$ and the effective tip field, which, in the presence of V_{RF} with frequency f, has a static component $\mathbf{B}_{tip}$ and an oscillatory component $\Delta\mathbf{B}_{tip}\cos(2\pi ft)$. The Hamiltonian is given by (*25*)

$$H = \gamma\hbar\left[\mathbf{B} + \Delta\mathbf{B}_{tip}\cos\left(2\pi ft\right)\right]\cdot\mathbf{S} \qquad (1)$$

where γ is the gyromagnetic ratio and $\hbar$ is Planck's constant. $\mathbf{B} = \mathbf{B}_{ext} + \mathbf{B}_{tip}$ is the total static field. As long as $\Delta\mathbf{B}_{tip}$ is non-collinear with $\mathbf{B}$, it can drive transitions between $|\downarrow\rangle$ and $|\uparrow\rangle$ states when hf matches the Zeeman splitting set by $\mathbf{B}$ (Fig. 1B, bottom). This change in magnetic states is visible as a change in the steady-state current in the CW-ESR spectrum (Fig. 1C).

To access the fast coherent spin dynamics of a Ti atom, we applied a series of RF pulses at the resonant frequency to induce Rabi oscillations between the two spin states (Figs. 1A and 2A). Between pulses, the Ti spin was reinitialized to the $|\downarrow\rangle$ state by a spin-polarized current. The degree of polarization of the initial state was determined by the spin polarization of the tip (*27*). During the RF pulse, the Ti spin rotated coherently between the $|\downarrow\rangle$ and $|\uparrow\rangle$ states at the Rabi frequency Ω, so increasing the pulse width τ yielded an oscillatory current signal ΔI (Fig. 2, A and B). The exponential decay of ΔI gives the coherence time $T_2^{\text{Rabi}} \approx 40$ ns. When the RF frequency was detuned away from the Larmor frequency, Ω increased and the oscillation amplitude was reduced (Fig. S10).

The Rabi oscillation of the Ti spin was read out magnetoresistively by using a homodyne detection technique (Fig. 2C and Supplementary Sec. 4), a standard technique for coherent detection in physics and engineering (*28, 29*). Here the asymmetric CW-ESR line shape is the result of homodyne demodulation (*26*). When the moment of the magnetic tip was canted with respect to the quantization axis of the Ti spin, the Larmor precession of the Ti spin yielded an RF conductance G_{RF}. The Rabi oscillations of the Ti spin modulated the amplitude of G_{RF}, and were then extracted by measuring the time-average current due to V_{RF} (Fig. 2C). This homodyne detection yielded better signal-to-noise ratio than measurements using DC pulses (Supplementary Sec. 5), so homodyne detection results are reported below.

The spatial orientation of the tip magnetic moment was crucial for observing the Rabi oscillations (Supplementary Sec. 6), because both the driving field and the amplitude of G_{RF} increased with the angle θ between the tip magnetic moment and $\mathbf{B}_{ext}$ (inset of Fig. 1C).

We gained additional control of Ω by adjusting the tip-atom distance d_{tip}, in addition to varying V_{RF}. Ω increased linearly with the setpoint current I_{DC} at a constant V_{DC} and V_{RF} (Fig. 2D). Because I_{DC} depended exponentially on d_{tip}, this result demonstrated the exponential dependence of Ω on d_{tip}, an important characteristic of exchange-field-driven ESR (*25*). We note that T_2^{Rabi} increased with larger d_{tip} (Fig. 2D), because one of the dominant decoherence sources was the

tunneling current (Supplementary Sec. 7) (*30*). For any given tip, T_2^{Rabi} and Ω scaled inversely with varying tip height. Thus, for a given tip and V_{DC}, the number of observable Rabi cycles was nearly independent of the tip height, and could possibly be increased by using the magnetic dipolar coupling to the tip, or by placing a surface spin nearby to supply the magnetic field gradient (*23*).

The coherence time of Rabi oscillations T_2^{Rabi} is, in principle, sensitive to (i) scattering electrons from tip or substrate (*31*), (ii) tunneling current arising through V_{DC} (*30*) and V_{RF}, (iii) variations of the resonant frequency caused by the slow-varying tip magnetic field, and (iv) variations in Ω caused by changes of tip-atom distance (Fig. 2D) or variations in V_{RF}. To understand and improve the spin coherence time, we applied multi-pulse spin manipulation sequences (Fig. 3).

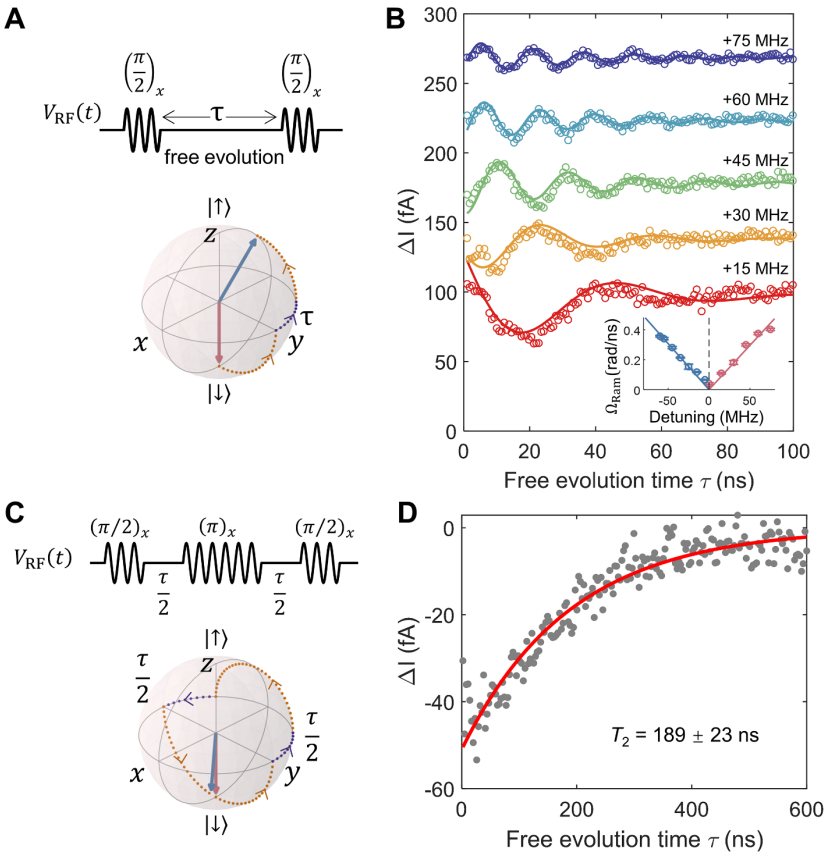

Fig. 3. Ramsey fringes and spin echo of a single Ti spin. (**A**) Pulse scheme (top) and Bloch sphere representation (bottom) of the spin evolution in the rotating frame for Ramsey fringes measurement. Red/blue arrow represents the Ti spin's initial/final state. Purple dots indicate free evolution between pulses. Orange dots represent a rotation about the *x* axis. (**B**) Ramsey signals and Ramsey fringe frequency Ω_{Ram} (inset) at different detuning frequencies $f - f_0$. (**C**) Pulse scheme (top) and Bloch sphere representation (bottom) for Hahn-echo measurement. (**D**) Spin-echo signals

at different total free evolution time τ. The exponential fit (red curve) gives a coherence time of T_2 ~189 ns. Measured at V_{DC} = 50 mV, I_{DC} = 3 pA; V_{RF} = 190 mV, f_0 = 20.55 GHz, B_{ext} = 0.82 T.

Figure 3B shows the Ramsey fringes measured on a single Ti atom by applying two π/2 pulses separated by a time delay τ, where π represents an RF pulse that flips the spin from |↓⟩ to |↑⟩. The RF frequency was intentionally detuned from the resonance so that during the free evolution τ, a phase was accumulated between the two spin components. The time delay τ thus determined whether the spin returned to the |↓⟩ state or continued to evolve to the |↑⟩ state, leading to interference fringes. We directly controlled the Ramsey fringe frequency by choosing the frequency detuning $f - f_0$ (Fig. 3B, inset).

The decay of the Ramsey signal with τ also gave a coherence time T_2^*, which was about 40 ns. T_2^* was not substantially longer than T_2^{Rabi}, indicating that decoherence was dominated by sources other than current induced by V_{RF} or slow variations in Ω.

To improve the coherence time, we performed a Hahn-echo pulse sequence, consisting of a π pulse placed between two π/2 pulses: π/2−τ/2−π−τ/2−π/2, where τ is the duration of free precession (Fig. 3C). This sequence decoupled the Ti spin from any slowly changing magnetic fields (*32*). Here the last π/2 pulse served as a homodyne detection pulse (*7*). The echo signal decayed exponentially with a time constant $T_2 \approx 189 \pm 23$ ns (Fig. 3D), which is several times longer than T_2^{Rabi} or T_2^*. This result indicates that the Ramsey coherence time T_2^* was limited by slow field variations that can be cancelled by the echo technique. The main remaining decoherence source is the tunneling current and scattering electrons from the tip and substrate, and thus we would expect lower tunnel current and thicker MgO (*31*) to further extend T_2.

We further demonstrate coherent operations on coupled-spin states in designed atomic structures by assembling Ti atom pairs at chosen spacings (Fig. 4) (*24*). The spin Hamiltonian of a Ti spin dimer ($\mathbf{S}_1$ and $\mathbf{S}_2$) is

$$H = H_{\text{Zee}} + H_{\text{int}} \qquad (2)$$

which consists of the Zeeman energy $H_{\text{Zee}} = \gamma\hbar\left(B_{\text{ext}} + B_{\text{tip}}\right)S_{1z} + \gamma\hbar B_{\text{ext}}S_{2z}$ and the interaction energy $H_{\text{int}} = J\mathbf{S}_1 \cdot \mathbf{S}_2 + D\left(3S_{1z}S_{2z} - \mathbf{S}_1 \cdot \mathbf{S}_2\right)$ (Supplementary Sec. 11) (*24*). The Ti spin under the tip is $\mathbf{S}_1$. H_{int} contains an exchange coupling with strength J and dipolar coupling with strength D,

and produced a four-level energy spectrum with an unequal energy spacing, which could be characterized by CW-ESR (*24, 26*).

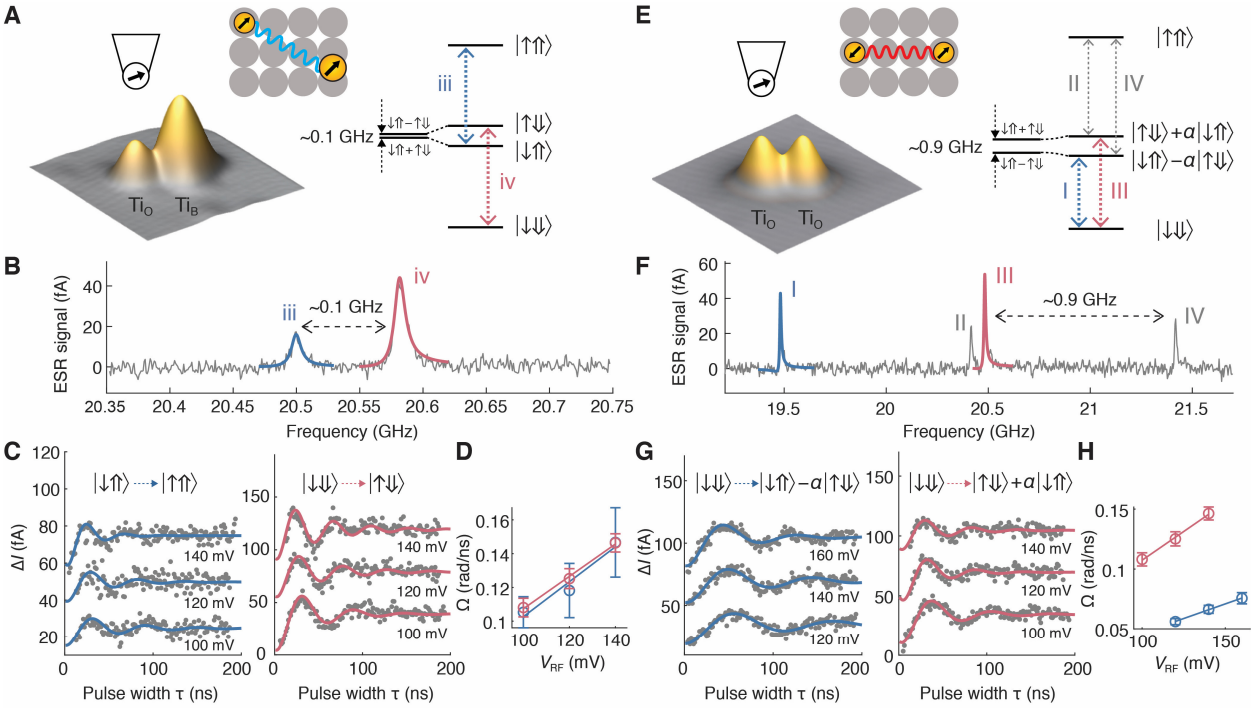

Fig. 4. Coherent control of spin dimers. (**A**) Left: Schematic showing an STM image (4 nm × 4 nm) of one oxygen-site and one bridge-site Ti atom (V_{DC} = 60 mV, I_{DC} = 30 pA), and the magnetic tip. Middle: atom positions of Ti dimer on MgO. Gray circles represent oxygen atoms. Right: energy level diagram with a ferromagnetic coupling of ~0.1 GHz. Dashed arrows indicate ESR transitions. (**B**) CW-ESR measured on the oxygen-site Ti atom (V_{DC} = 50 mV, I_{DC} = 3 pA, V_{RF} =10 mV). (**C**) Pulsed ESR measured on the oxygen-site Ti atom at f = 20.50 GHz and 20.58 GHz, corresponding to the blue and red peaks in (B) (V_{DC} = 50 mV, I_{DC} = 3 pA), showing the coherent transitions from $|\downarrow\Uparrow\rangle$ to $|\uparrow\Uparrow\rangle$ (left), and from $|\downarrow\Downarrow\rangle$ to $|\uparrow\Downarrow\rangle$ (right). (**D**) Dependence of **Ω** on V_{RF} for transitions iii and iv. **Ω** is extracted from a sinusoidal fit in (C). (**E-H**) same as (A−D) except measured on two oxygen-site Ti atoms having a closer spacing, with an anti-ferromagnetic coupling of ~0.9 GHz. (G) shows the coherent transitions from $|\downarrow\Downarrow\rangle$ to $|\downarrow\Uparrow\rangle - \alpha|\uparrow\Downarrow\rangle$ (left) and from $|\downarrow\Downarrow\rangle$ to $|\uparrow\Downarrow\rangle + \alpha|\downarrow\Uparrow\rangle$ (right), where $\alpha \approx 0.7$. (H) shows dependence of **Ω** on V_{RF} for transitions I and III. V_{RF} = 25 mV in (F). Measured at B_{ext} = 0.82 T.

The spin dimer in Fig. 4A had an interaction energy of ~0.1 GHz, much smaller than the Zeeman energy difference between the two spins induced by the tip field (~0.35 GHz). The energy eigenstates thus remained approximated as Zeeman product states ($|\downarrow\Downarrow\rangle$, $|\downarrow\Uparrow\rangle$, $|\uparrow\Downarrow\rangle$ and $|\uparrow\Uparrow\rangle$) (*24*). We performed controlled rotation of the spin under the tip (target spin), conditionally on the state of the other spin (control spin). When a pulse was applied at frequency f_{iv} (Fig. 4B), matching the energy spacing between the first and third energy levels (Fig. 4A, right panel), only the $|\downarrow\Downarrow\rangle \dashrightarrow$

$|\uparrow\Downarrow\rangle$ transition was resonant with RF field. Correspondingly, the RF field flipped the target spin if, and only if, the control spin was in state $|\Downarrow\rangle$ (Fig. 4C, right panel). Similarly, a π pulse at frequency f_{iii} flipped the target spin when the control spin was in state $|\Uparrow\rangle$. This capability provides a possible realization of a CNOT gate (*33*).

The spin dimer in Fig. 4E had a larger interaction of ~0.9 GHz, which overcame the magnetic asymmetry created by the tip, and caused two of the quantum eigenstates to strongly mix to form states $|\downarrow\Uparrow\rangle-\alpha|\uparrow\Downarrow\rangle$ and $|\uparrow\Downarrow\rangle+\alpha|\downarrow\Uparrow\rangle$ with $\alpha \approx 0.7$ (*24*). The other two eigenstates remained the Zeeman product states (Fig. 4E, right panel). We coherently excited the system from the ground state $|\downarrow\Downarrow\rangle$ to either of the mixed states. When the RF pulse was tuned to transition I (Fig. 4F), $|\downarrow\Downarrow\rangle$ evolved into $|\downarrow\Uparrow\rangle-\alpha|\uparrow\Downarrow\rangle$ for a π pulse (Fig. 4G, left). In comparison, an RF pulse at the frequency of transition III coherently rotated $|\downarrow\Downarrow\rangle$ into $|\uparrow\Downarrow\rangle+\alpha|\downarrow\Uparrow\rangle$ (Fig. 4G, right). The Rabi frequency Ω grew in proportion to V_{RF} for these two transitions (Fig. 4H). For any given V_{RF}, the ratio of Ω for these two transitions depended only on the state mixing α (Supplementary Sec. 11). As we increased the tip field, the state mixing was reduced (*24*), and thus the ratio of Ω between I and III became smaller (Fig. S13). This tunable tip magnetic field thus provided control of the energy-level structures and Rabi rates.

Combining pulsed ESR with STM manipulation paves the way for the coherent excitation and detection of many-body states of artificial spin structures, such as topological quantum states of atomic chains (*34*). The exchange-field-driven coherent manipulation should be applicable to other solid-state spin systems (Fig. S14) (*5*, *7*). The time-domain ESR spectroscopy could extend the sensing capabilities of a single-atom quantum sensor (*8, 9, 32*) and possibly also be used for quantum information applications using surface atoms (*33, 35*).

References and Notes:

1. T. Fukuhara *et al.*, *Nature* **502**, 76-79 (2013).
2. C. Senko *et al.*, *Science* **345**, 430-433 (2014).
3. A. Abragam, B. Bleaney, *Electron Paramagnetic Resonance of Transition Ions*. (Oxford Univ. Press, Oxford, 2012).
4. S. Schlauderer *et al.*, *Nature* **569**, 383-387 (2019).
5. S. Thiele *et al.*, *Science* **344**, 1135-1138 (2014).

6. K. C. Nowack, F. H. L. Koppens, Y. V. Nazarov, L. M. K. Vandersypen, *Science* **318**, 1430-1433 (2007).
7. J. J. Pla *et al.*, *Nature* **489**, 541-545 (2012).
8. J. R. Maze *et al.*, *Nature* **455**, 644-647 (2008).
9. G. Balasubramanian *et al.*, *Nature* **455**, 648-651 (2008).
10. G. Czap *et al.*, *Science* **364**, 670-673 (2019).
11. C. F. Hirjibehedin, C. P. Lutz, A. J. Heinrich, *Science* **312**, 1021-1024 (2006).
12. S. Loth, M. Etzkorn, C. P. Lutz, D. M. Eigler, A. J. Heinrich, *Science* **329**, 1628-1630 (2010).
13. S. Yoshida *et al.*, *Nat. Nanotechnol.* **9**, 588-593 (2014).
14. A. A. Khajetoorians *et al.*, *Science* **339**, 55-59 (2013).
15. T. L. Cocker, D. Peller, P. Yu, J. Repp, R. Huber, *Nature* **539**, 263-267 (2016).
16. S. Li, S. Chen, J. Li, R. Wu, W. Ho, *Phys. Rev. Lett.* **119**, 176002 (2017).
17. A. A. Khajetoorians *et al.*, *Nat. Phys.* **8**, 497-503 (2012).
18. R. Toskovic *et al.*, *Nat. Phys.* **12**, 656-660 (2016).
19. R. Drost, T. Ojanen, A. Harju, P. Liljeroth, *Nat. Phys.* **13**, 668-671 (2017).
20. A. J. Heinrich, J. A. Gupta, C. P. Lutz, D. M. Eigler, *Science* **306**, 466-469 (2004).
21. F. Meier, L. Zhou, J. Wiebe, R. Wiesendanger, *Science* **320**, 82-86 (2008).
22. S. Baumann *et al.*, *Science* **350**, 417-420 (2015).
23. F. D. Natterer *et al.*, *Nature* **543**, 226-228 (2017).
24. K. Yang *et al.*, *Phys. Rev. Lett.* **119**, 227206 (2017).
25. K. Yang *et al.*, *Phys. Rev. Lett.* **122**, 227203 (2019).
26. Y. Bae *et al.*, *Sci. Adv.* **4**, eaau4159 (2018).
27. S. Loth *et al.*, *Nat. Phys.* **6**, 340-344 (2010).
28. C. Gross *et al.*, *Nature* **480**, 219-223 (2011).
29. N. Lee *et al.*, *Science* **332**, 330-333 (2011).
30. P. Willke *et al.*, *Sci. Adv.* **4**, eaaq1543 (2018).
31. W. Paul *et al.*, *Nat. Phys.* **13**, 403-407 (2017).
32. C. L. Degen, F. Reinhard, P. Cappellaro, *Rev. Mod. Phys.* **89**, 035002 (2017).
33. A. Gaita-Ariño, F. Luis, S. Hill, E. Coronado, *Nat. Chem.* **11**, 301-309 (2019).
34. S. Nadj-Perge *et al.*, *Science* **346**, 602-607 (2014).
35. D. M. Zajac *et al.*, *Science* **359**, 439-442 (2018).
36. P. Willke et al., *Science* **362**, 336-339 (2018).
37. W. Paul, S. Baumann, C. P. Lutz, A. J. Heinrich, *Rev. Sci. Instrum.* **87**, 074703 (2016).

38. R. Wiesendanger, *Rev. Mod. Phys.* **81**, 1495-1550 (2009).
39. M. Ternes, *New J. Phys.* **17**, 063016 (2015).
40. F. Delgado, J. Fernández-Rossier, *Prog. Surf. Sci.* **92**, 40-82 (2017).
41. C. Godfrin *et al.*, *Phys. Rev. Lett.* **119**, 187702 (2017).
42. E. Kawakami *et al.*, *Nat. Nanotechnol.* **9**, 666-670 (2014).
43. S. Yan, D.-J. Choi, A. J. BurgessJacob, S. Rolf-Pissarczyk, S. Loth, *Nat. Nanotechnol.* **10**, 40-45 (2015).
44. J. L. Lado, A. Ferrón, J. Fernández-Rossier, *Phys. Rev. B* **96**, 205420 (2017).
45. C. P. Slichter, *Principles of Magnetic Resonance*. (Springer, 1996).
46. K. Yang et al., *Nat. Nanotechnol.* **13**, 1120-1125 (2018).

Acknowledgments: We thank Bruce Melior for expert technical assistance. **Funding:** We acknowledge financial support from the Office of Naval Research. S-H.P., P.W., Y.B., T.C., T.E. and A.J.H acknowledge support from Institute for Basic Science (IBS-R027-D1). A.A. acknowledges support from the Engineering and Physical Sciences Research Council (EP/L011972/1 and EP/P000479/1), and the QuantERA European Project SUMO. **Authors contributions:** K.Y. and C.P.L. designed the experiment. K.Y., W.P., S-H.P., P.W., Y.B., T.C. and T.E. performed STM measurements. K.Y. and C.P.L. performed the analysis and wrote the manuscript with help from all authors. All authors discussed the results and edited the manuscript. **Competing interests:** None declared. **Data and materials availability:** All data needed to evaluate the conclusions in the paper are present in the paper and/or the Supplementary Materials. Additional data related to this paper may be requested from the authors.

Supplementary Materials:

Materials and Methods

Supplementary Text

Figures S1-S14

References (*36-46*)

Science
AAAS

Supplementary Materials for

Coherent spin manipulation of individual atoms on a surface

Kai Yang[1,*], William Paul[1], Soo-Hyon Phark[1,2,3], Philip Willke[1,2,4], Yujeong Bae[1,2,4], Taeyoung Choi[2,3], Taner Esat,[1,2,4] Arzhang Ardavan,[5] Andreas J. Heinrich[2,3,*], and Christopher P. Lutz[1,*]

Correspondence to: k.yang@ibm.com; heinrich.andreas@qns.science; cplutz@us.ibm.com

This PDF file includes:

Materials and Methods

Measurements were performed in a home-built ultrahigh-vacuum ($< 10^{-9}$ Torr) STM operating at 1.2 K. Bilayer MgO was grown on an atomically clean Ag(001) single crystal by thermally evaporating Mg in an O_2 environment (*31*). Ti and Fe atoms were deposited *in situ* from pure metal rods by e-beam evaporation onto the sample held at ~10 K. Our previous study showed that Ti atoms studied here were most likely hydrogenated (*24*). DFT calculations (*24*) shows that clean Ti on MgO has a spin of 1, and the hybridization of the H with the Ti *d* orbitals results in an equivalent $3d^1$ configuration of Ti, and thus spin-1/2. Considering that hydrogen is the predominant component of the residual gas, and the high affinity of Ti for H in various environments, it is most likely the Ti atoms were hydrogenated. In addition, only Ti isotopes having zero nuclear spin were investigated (*36*). Fig. S1A shows a large scale STM images of our sample with atoms adsorbed on MgO/Ag(001). An external magnetic field (0.82 T or 0.90 T as indicated in the figure captions) was applied which was ~8° off the surface with the in-plane component aligned along the [100] direction of the MgO lattice. STM images were acquired in constant-current mode and all voltages refer to the sample voltage with respect to the tip.

The iridium STM tip was coated with silver by indentations into the Ag sample until the tip gave a good lateral resolution in the STM image. To prepare a spin-polarized tip, Fe atoms on MgO were transferred onto the tip by applying a bias voltage (~0.55 V) while withdrawing the tip from near point contact with the Fe atom. The degree of spin polarization was verified by the asymmetry in dI/dV spectra of Ti with respect to voltage polarity (*24*).

The continuous-wave electron spin resonance (CW-ESR) spectra were acquired by sweeping the frequency of an RF voltage V_{RF} generated by the RF generator (Agilent E8257D) across the tunneling junction and monitoring changes in the tunneling current. The current signal was modulated at 95 Hz by chopping V_{RF}, which allowed readout of the current by a lock-in technique (*22*). All measurements are for hydrogenated Ti atom bound to an oxygen site of the MgO. For pulsed-ESR measurements (Fig. S1B), the frequency and amplitude of the RF voltage were set to constant values as indicated in the figure captions, and the RF generator was gated by an arbitrary waveform generator (Tektronix AWG7122C) to generate RF pulses. The current signal during pulsed-ESR measurements was modulated at 818 Hz and read out by a lock-in technique. The RF and DC voltages were combined at room temperature using an RF diplexer, and guided to the STM tip through semi-rigid coaxial cables with a loss of ~30 dB at 20 GHz (*37*).

In addition to Ti atoms, we also performed pulsed-ESR measurement on single Fe atoms on MgO as shown in Fig. S14.

Supplementary Text

Section 1. Characterization of the pulsed RF output

Before we applied the RF pulses into the STM junction, we used an RF diode (Agilent 8473C) to characterize the RF pulses at room temperature. As shown in Fig. S2, the lock-in output varies linearly with the pulse width of the gating voltage for a fixed RF power, indicating the RF pulse width also varies linearly with the pulse width of the gating voltage. A larger RF power results in a proportionally larger lock-in output.

Section 2. Alignment of RF and DC pulses

The RF and DC pulses travel along different electrical paths in our set-up until they are combined at the RF diplexer. This, together with the possible time delay between the gating and RF output of the high-frequency source, could result in a misalignment of the RF and DC pulses in the time domain. Using a single Fe atom as an atomic-scale rectifier, we characterized the time misalignment between the RF and DC pulses. As shown in Fig. S3A, we varied the time delay between the DC pulse (15 mV and 2 ns in width) and an RF gating pulse (150 ns in width), and measured the lock-in output. When the DC pulse overlaps with the ~28 mV RF pulse, the lock-in shows the non-linearity of *I*-*V* curve of the Fe atom at 15 mV; when they do not overlap, the lock-in shows the non-linearity at 0 mV. The difference in the non-linearity at different DC voltages thus gives us the signal contrast to measure the alignment (Δt) of the DC and the RF pulse, which is ~100 ns in our STM set-up. This time delay was then compensated in the pulsed experiments.

Section 3. d*I*/d*V* spectra of Ti on MgO

The d*I*/d*V* spectra on the Ti atom show a pair of conductance steps placed symmetrically about zero bias (Fig. S4), which originates from spin-flip excitations. The asymmetry of step heights for opposite voltage polarities is due to the selection rule for spin excitations (*27*). The ratio of the step heights yields the magnitude and sign of the spin polarization of the magnetic tip (*27*), which we find to be typically 15–35% for Fe-terminated tips.

Section 4. Homodyne detection of Rabi oscillations

In this section, we discuss the detection mechanism of the pulsed ESR signals. The spin Hamiltonian of Ti influenced by an RF voltage at frequency *f* is (*25*):

$$H = \gamma\hbar\left[\mathbf{B} + \Delta\mathbf{B}_{\mathrm{tip}}\cos(2\pi f t)\right]\cdot\mathbf{S} \qquad \text{(S1)}$$

The first term determines the quantization axis of the Ti spin, which is along the direction of the total magnetic field $\mathbf{B} = \mathbf{B}_{\mathrm{ext}} + \mathbf{B}_{\mathrm{tip}}$. The tip field $\mathbf{B}_{\mathrm{tip}}$ is tilted with respect to $\mathbf{B}$ by an angle θ, which can be determined from the experiments (see Section 8). The oscillating tip field $\Delta\mathbf{B}_{\mathrm{tip}}\cos(2\pi f t)$ has a component $\Delta B_{\mathrm{tip}}^{\perp}\cos(2\pi f t)$ that is perpendicular to $\mathbf{B}$, which corresponds to $B_{\mathrm{AC}}(t)$ that drives the spin resonance.

When performing pulsed ESR measurement, the tip field $B_{\mathrm{tip}} \ll B_{\mathrm{ext}}$, and thus the quantization axis is close to the external field direction *z*. We define the plane spanned by the two vectors $\mathbf{B}_{\mathrm{ext}}$ and $\mathbf{B}_{\mathrm{tip}}$ as the *xz* plane (Fig. S5A).

We first consider the simple case without spin decoherence. The following analysis shows that the measured lock-in signal is sinusoidal with a background slope and offset. Assuming at $t = 0$, the Ti spin is in state $\left|\tilde{\phi}(t=0)\right\rangle = |\downarrow\rangle$. In the rotating frame, this spin vector rotates around the direction $(\Omega, 0, \omega_0 - \omega)$. Here Ω is the Rabi frequency, ω_0 is the Larmor frequency and $\omega = 2\pi f$ is the angular frequency of the RF voltage. When the RF field is in resonance with the Zeeman energy ($\omega = \omega_0$), the spin state in the rotating frame at time *t* is:

$$\left|\tilde{\phi}(t)\right\rangle = \sin\frac{\Omega t}{2}|\uparrow\rangle + i\cos\frac{\Omega t}{2}|\downarrow\rangle \qquad \text{(S2)}$$

In the lab frame, the state is

$$|\phi(t)\rangle = e^{-i\omega t S_{\mathrm{Ti}}^z}\left|\widetilde{\phi}(t)\right\rangle = e^{-i\omega t/2}\sin\frac{\Omega t}{2}|\uparrow\rangle + e^{i\omega t/2}\, i\cos\frac{\Omega t}{2}|\downarrow\rangle \tag{S3}$$

Thus, the expectation values of the Ti spin $\langle \boldsymbol{S}_{\mathrm{Ti}}\rangle$ in the lab frame are

$$\begin{aligned}\langle S_{\mathrm{Ti}}^x\rangle &= -\frac{1}{2}\sin\Omega t\cdot\sin\omega t\\ \langle S_{\mathrm{Ti}}^y\rangle &= \frac{1}{2}\sin\Omega t\cdot\cos\omega t\\ \langle S_{\mathrm{Ti}}^z\rangle &= -\frac{1}{2}\cos\Omega t\end{aligned} \tag{S4}$$

The spin-polarized junction conductance depends on the relative orientation of the tip spin and the Ti spin: $G = G_{\mathrm{junc}}(1 + a\langle \mathbf{S}_{\mathrm{t}}\rangle\cdot\langle \mathbf{S}_{\mathrm{Ti}}\rangle)$ (*38*). Here a is a normalization factor that relates the quantum-mechanical transition intensities to observable tunneling probabilities, and G_{junc} is the spin-averaged conductance. The total voltage across the junction consists of DC and RF parts: $V = V_{\mathrm{DC}} + V_{\mathrm{RF}}(t) = V_{\mathrm{DC}} + V_{\mathrm{RF}}\cos(\omega t + \varphi_{\mathrm{RF}})$, where φ_{RF} accounts for the phase difference between the applied RF voltage and the precession of the Ti spin in the lab frame. The tip spin $\langle \boldsymbol{S}_{\mathrm{t}}\rangle$ has a constant z component $\langle S_{\mathrm{t}}^z\rangle$, and a constant x component $\langle S_{\mathrm{t}}^x\rangle$. The tunneling current can thus be written as:

$$\begin{aligned}I(t) = GV = G_{\mathrm{junc}}V_{\mathrm{DC}}&\left[1 - \frac{1}{2}a\langle S_{\mathrm{t}}^x\rangle\sin\Omega t\cdot\sin\omega t - \frac{1}{2}a\langle S_{\mathrm{t}}^z\rangle\cos\Omega t\right]\\ &+ G_{\mathrm{junc}}V_{\mathrm{RF}}\cos(\omega t + \varphi_{\mathrm{RF}})\left[1 - \frac{1}{2}a\langle S_{\mathrm{t}}^x\rangle\sin\Omega t\cdot\sin\omega t - \frac{1}{2}a\langle S_{\mathrm{t}}^z\rangle\cos\Omega t\right]\end{aligned} \tag{S5}$$

Discarding terms that give zero when time-averaged over a cycle of the RF voltage leaves $I(t) = I(t)_{\mathrm{DC}} + I(t)_{\mathrm{homo}}$, where the current due to V_{DC} is

$$I(t)_{\mathrm{DC}} = G_{\mathrm{junc}}V_{\mathrm{DC}}\left(1 - \frac{1}{2}a\langle S_{\mathrm{t}}^z\rangle\cos\Omega t\right) \tag{S6}$$

and the current due to V_{RF}, called the homodyne component, is

$$\begin{aligned}I(t)_{\mathrm{homo}} &= V_{\mathrm{RF}}(t)\cdot G_{\mathrm{RF}}(t)\\ &= V_{\mathrm{RF}}\cos(\omega t + \varphi_{\mathrm{RF}})\cdot\left(-G_{\mathrm{junc}}\frac{1}{2}a\langle S_{\mathrm{t}}^x\rangle\sin\Omega t\cdot\sin\omega t\right)\\ &= -G_{\mathrm{junc}}V_{\mathrm{RF}}\frac{1}{2}a\langle S_{\mathrm{t}}^x\rangle\sin\Omega t\cdot\sin\omega t\cdot\cos(\omega t + \varphi_{\mathrm{RF}})\\ &= -G_{\mathrm{junc}}V_{\mathrm{RF}}\frac{1}{2}a\langle S_{\mathrm{t}}^x\rangle\sin\Omega t\cdot\frac{1}{2}[-\sin\varphi_{\mathrm{RF}} + \sin(2\omega t + \varphi_{\mathrm{RF}})]\end{aligned} \tag{S7}$$

The time-averaged tunneling current for a Rabi measurement with a pulse width τ and pulse repetition period τ_{r} used in lock-in A-cycle (Fig. S1B) is then:

$$\begin{aligned}\overline{I_{\mathrm{A}}} = \frac{1}{\tau_{\mathrm{r}}}\int_0^{\tau}(I(t)_{\mathrm{DC}} + I(t)_{\mathrm{homo}})\,dt + \frac{1}{\tau_{\mathrm{r}}}\int_{\tau}^{\tau_{\mathrm{r}}} G_{\mathrm{junc}}V_{\mathrm{DC}}\left\{1 - \frac{1}{2}a\langle S_{\mathrm{t}}^z\rangle\left[1 + (\cos\Omega\tau - 1)\mathrm{e}^{-\frac{t-\tau}{T_1}}\right]\right\}dt\\ \approx \frac{1}{\tau_{\mathrm{r}}}\left[G_{\mathrm{junc}}\frac{V_{\mathrm{RF}}}{\Omega}\frac{1}{4}a\langle S_{\mathrm{t}}^x\rangle\sin\varphi_{\mathrm{RF}}\,(1 - \cos\Omega\tau)\right]\\ + \frac{1}{\tau_{\mathrm{r}}}G_{\mathrm{junc}}V_{\mathrm{DC}}\left\{\tau_{\mathrm{r}}\left(1 - \frac{1}{2}a\langle S_{\mathrm{t}}^z\rangle\right) + \tau\frac{1}{2}a\langle S_{\mathrm{t}}^z\rangle - \frac{1}{2}a\langle S_{\mathrm{t}}^z\rangle\left[\frac{\sin\Omega\tau}{\Omega} + (\cos\Omega\tau - 1)T_1\right]\right\}\end{aligned} \tag{S8}$$

The time-averaged tunneling current in B-cycle (Fig. S1B), in which $V_{\mathrm{RF}} = 0$, is

$$\overline{I_{\mathrm{B}}} = G_{\mathrm{junc}}V_{\mathrm{DC}}\left(1 - \frac{1}{2}a\langle S_{\mathrm{t}}^z\rangle\right) \tag{S9}$$

The lock-in amplifier measures the difference in the averaged current in A and B cycles, which is

$$(\overline{I_{\mathrm{A}}} - \overline{I_{\mathrm{B}}}) = k_{\mathrm{RF}}(1 - \cos\Omega\tau) + k_{\mathrm{DC}}[-\sin\Omega\tau + \Omega T_1(1 - \cos\Omega\tau)] + k_{\mathrm{lin}}\tau \tag{S10}$$

where $k_{\mathrm{RF}} = \frac{aG_{\mathrm{junc}}}{4}\frac{V_{\mathrm{RF}}}{\Omega\tau_{\mathrm{r}}}\sin\varphi_{\mathrm{RF}}\langle S_{\mathrm{t}}^{x}\rangle$, $k_{\mathrm{DC}} = \frac{aG_{\mathrm{junc}}}{2}\frac{V_{\mathrm{DC}}}{\Omega\tau_{\mathrm{r}}}\langle S_{\mathrm{t}}^{z}\rangle$, and $k_{\mathrm{lin}} = \frac{aG_{\mathrm{junc}}}{2}\frac{V_{\mathrm{DC}}}{\tau_{\mathrm{r}}}\langle S_{\mathrm{t}}^{z}\rangle$.

Considering further the RF rectified current due to the non-linearity in the *I-V* curve (*37*) of the Ti atom, the lock-in signal is then:

$$V_{\mathrm{lock-in}}(\tau) \propto k_{\mathrm{RF}}(1-\cos\Omega\tau) + k_{\mathrm{DC}}[-\sin\Omega\tau + \Omega T_1(1-\cos\Omega\tau)] + (k_{\mathrm{lin}}+k_{\mathrm{rec}})\tau$$
$$\propto -\sqrt{(k_{\mathrm{RF}}+k_{\mathrm{DC}}\Omega T_1)^2 + k_{\mathrm{DC}}^2}\sin(\Omega\tau+\alpha) + (k_{\mathrm{lin}}+k_{\mathrm{rec}})\tau + k_{\mathrm{DC}}\Omega T_1 + k_{\mathrm{RF}} \quad \text{(S11)}$$

where $\tan\alpha = (k_{\mathrm{RF}} + k_{\mathrm{DC}}\Omega T_1)/k_{\mathrm{DC}} = \frac{\sin\varphi_{\mathrm{RF}}}{2}\frac{V_{\mathrm{RF}}}{V_{\mathrm{DC}}}\tan\theta + \Omega T_1$. Here θ is the tilting angle of the tip magnetic moment with respect to the direction of the external field, i.e. $\tan\theta = \frac{\langle S_{\mathrm{t}}^{x}\rangle}{\langle S_{\mathrm{t}}^{z}\rangle}$.

When the tip spin is perpendicular to the external field, i.e. $\theta = \pi/2$, there is only homodyne detection ($k_{\mathrm{DC}} = k_{\mathrm{lin}} = 0$), and the lock-in signal is then

$$V_{\mathrm{lock-in,homo}}(\tau) \propto k_{\mathrm{rec}}\tau + k_{\mathrm{RF}}(1-\cos\Omega\tau) \quad \text{(S12)}$$

Note that if the tip spin is fully aligned with the external field, there is no effective AC magnetic field to drive the ESR of the Ti atom, i.e. $\Omega = 0$. Thus, there is no pure DC detection case.

The quantum decoherence modulates the Rabi oscillation with an exponential factor, and we used the further simplified equation (S13) to fit the Rabi oscillations, and removed the linear slope in the figures in the manuscript, using

$$V_{\mathrm{lock-in}}(\tau) \approx k_1 e^{-\frac{\tau}{T_2}}\sin(\Omega\tau+\tilde{\alpha}) + k_2\tau + k_3 \quad \text{(S13)}$$

The homodyne detection mechanism can also be seen in the CW-ESR spectra of a single Ti spin (Fig. 1C and Fig. S6) (*24, 26*). The ESR lineshape is described by

$$I^{\mathrm{ESR}} = I_0 + I_R \cdot \frac{1+q\cdot\delta}{1+\delta^2} \quad \text{(S14)}$$

where q is a parameter related to the phase difference between the RF voltage and the precession of the Ti spin, I_0 accounts for the background current due to the non-linearity of the junction conductance, and $\delta = (f_{\mathrm{RF}} - f_0)/(\Gamma/2)$ is the normalized frequency. Γ and I_R are the full width at half-maximum (FWHM) and the amplitude of the resonance, respectively:

$$\Gamma = \frac{1}{\pi T_2}\sqrt{1+\Omega^2 T_1 T_2} \quad \text{(S15)}$$

$$I_R = I_p\frac{\Omega^2 T_1 T_2}{\sqrt{1+\Omega^2 T_1 T_2}} \quad \text{(S16)}$$

As shown in Fig. S6B, q is small at small V_{RF}, and the ESR lineshape has a symmetric Lorentzian lineshape. With increasing V_{RF} and thus q, the ESR lineshape becomes more asymmetric due to the homodyne detection of the steady state precession of the Ti spin driven by the RF voltage.

Section 5. Different pulse schemes

In this section, we compare the three different schemes of pulse sequences (Fig. S7), which are sensitive to either the homodyne or DC detection of the Rabi signals. Here V_{DC} refers to both a constant DC voltage and to the constant-voltage pulses as shown.

In the homodyne detection scheme without DC pulses (Fig. S7A, top panel), a constant V_{DC} (~ 50 mV) is applied in the STM junction. This constant V_{DC} is used to initialize the Ti spin by

the spin-polarized current (*27*) during the time between two RF pulses. The DC current due to V_{DC} also causes some unintended decoherence during the coherent manipulations. Both V_{RF} and V_{DC} contribute to the lock-in signals of the detected Rabi oscillation as shown in (S11).

In the homodyne detection scheme with DC pulses (Fig. S7A, middle panel), a DC pulse is applied before the RF pulse to initialize the Ti spin. In this case, only the homodyne detection by V_{RF} contributes to the lock-in signals.

In the DC detection scheme with two DC pulses (Fig. S7A, bottom panel), a DC initialization pulse as well as a DC detection pulse are applied before and after the RF pulse, respectively. Since V_{RF} is not modulated at the lock-in frequency in this case, only the DC detection by V_{DC} contributes to the lock-in signals.

We showed the corresponding measured lock-in signals for the three pulse schemes in Fig. S7B, which displayed better signal-noise-ratios for the first two schemes. In most of our pulsed-ESR measurement, we used the first pulse scheme.

In all schemes we employ the time-average tunnel current due to V_{DC} (and due to the DC pulses when present) as a feedback signal to stabilize the tip-Ti distance. Since the effective magnetic field applied on the Ti spin varies exponentially with the tip-Ti distance, this is crucial for increasing the spin coherence time by maintaining a relatively constant resonant frequency during the data collections (typically 15 min to 2 hours).

Note that for the Ti on MgO under the setpoint conditions used in our experiment, the Ti spin is initialized by the spin-polarized tunnelling current, since the exchange scattering with tunnelling electrons occurs more frequently than the spin relaxation driven by the substrate or tip electrons (see Section 7). Successive RF pulses were separated by several T_1 times of Ti atoms.

The DC voltage was always on through the Ramsey and spin echo measurements. Thus the Ti spin was influenced by the DC current during the free evolution time. The tunneling current acts as a decoherence source during the free evolution time.

.

Section 6. Pulsed ESR measurements with different STM tips

The large Ω in our experiment was obtained by choosing tip terminations giving a large effective magnetic field perpendicular to the spin quantization axis of the Ti atom. During our experiment, we made eleven different spin-polarized STM tips in total. The number of Fe atoms attached to the STM apex varied from 1 to 6. All of these STM tips were capable of obtaining the CW-ESR spectra of Ti atoms, and four of them showed usable Rabi signals on the Ti atoms. These four tips were used to collect the data displayed in the manuscript. We labelled these four tips as #1, #2, #3 and #4, which had 4, 4, 5, 6 Fe atoms at the tip apex, respectively. Data in Figs. 2A and 2B were taken with tip #1; data in Fig. 1C were taken with tip #3; data in Figs. 2D, Fig. 3 and Fig. 4 were taken with tip #4. Fig. S8 shows the Rabi frequency Ω and spin decoherence time T_2^{Rabi} as a function of V_{RF} for these four different STM tips, obtained by fitting the Rabi oscillations of a single Ti atom on MgO.

Section 7. Decoherence sources of the Ti spin on MgO

In this section, we discuss two major sources of decoherence of the Ti spin on MgO/Ag(001). Under most conditions, the tunneling current is the major source of decoherence (*30*), as shown in Fig. 2D. The exchange scattering with tunnelling electrons occurs more frequently than the spin relaxation driven by the substrate electrons (which originate from Ag

and return to Ag) (*31*). The latter corresponds to a scattering current of $\frac{k_B T}{e} \cdot \frac{{G_s}^2}{G_0} \approx 10$ fA, as estimated using the theory of ref (*31*) using the point contact conductance ($G_s \approx 0.1\ \mu S$) of the Ti-MgO-Ag junction and at $T = 1.2$ K. Thus, the corresponding decoherence rate is negligible compared to the decoherence due to tunneling current (> 1 pA). The tip-Ti-tip scattering can also be omitted since the corresponding scattering current is $\frac{k_B T}{e} \cdot \frac{G_0 G^2}{{G_s}^2} \approx 10$ fA.

Figure 2D shows that the decoherence rate $1/T_2^{\text{Rabi}}$ has a linear dependence on the tunneling current. We understand this linear dependence as follows. The scattering between the tunneling electron ($\boldsymbol{\sigma}$) and the Ti spin can be described by a Kondo type interaction: $\mathbf{S} \cdot \boldsymbol{\sigma}$ (*27, 39*). This interaction acts as a stochastic magnetic field applied on the Ti spin, and thus each tunneling event could induce a phase shift in the atomic wave function with a certain probability. The decoherence rate due to the random field is proportional to the number of decoherence events per unit time (*30, 40*). This depends on two factors: the rate at which electrons available for scattering impinge on the Ti atom (which is dominated by the tunnelling current for the Ti atom on MgO in our STM junction), and the probability that the Ti spin transition occurs per impinging electron, which is close to unity as estimated from Fig. 2D. Thus, the decoherence rate is also proportional to the tunnelling current.

In addition to the tunneling current, our spin-echo measurement (Fig. 3D) suggests that the low-frequency magnetic field noise due to the relative motion between the magnetic tip and the Ti atom is the other major source of decoherence in the current experiment.

Note that a figure such as Fig. 2A was generated by averaging many measurements for each pulse width (τ) using the pulse scheme shown in Fig. S1B. The measurements typically consists of ~10 sweeps each averaging for ~1 s at each data point, to give ~10 s averaging time for each point presented. Thus, the decay of measured Rabi oscillations is, in principle, sensitive to: (a) genuine intrinsic dephasing (i.e. a loss of phase on the timescale of a single shot by decoherence sources such as scattering electrons); and (b) temporal ensemble average of many Rabi oscillations over many shots, and the decay of Rabi signal could result from slow fluctuations of the resonant frequency shot-to-shot due to the slow-varying tip magnetic field, and also slow variations in the Rabi rate Ω shot-to-shot. The spin-echo experiment can cancel these slow variations and thus give improved measured coherence time.

Section 8. Characterizing the tip-atom exchange interaction

The coherent Rabi oscillations of Ti spin on MgO is driven by the effective magnetic field from the STM tip (*25*). The direction of the tip magnetic field can be obtained as follows.

The total Zeeman energy (E_{total}) experienced by the Ti atom, including the contributions from both $\mathbf{B}_{\text{ext}}$ and $\mathbf{B}_{\text{tip}}$:

$$E_{\text{total}}(z) = \sqrt{E_{\text{ext}}^2 + E_{\text{tip}}^2(z) + 2E_{\text{ext}}E_{\text{tip}}(z)\cos\theta} \qquad \text{(S17)}$$

Here $E_{\text{ext}} = \gamma\hbar B_{\text{ext}}$ is the Zeeman energy due to $\mathbf{B}_{\text{ext}}$, and $E_{\text{tip}}(z) = \gamma\hbar B_{\text{tip}}(z) \propto \exp(-z/d_{\text{ex}})$ is the Zeeman energy due to $\mathbf{B}_{\text{tip}}$ (in the absence of $\mathbf{B}_{\text{ext}}$). θ is the angle between $\mathbf{B}_{\text{ext}}$ and $\mathbf{B}_{\text{tip}}$. At constant DC voltage, we use the approximation $E_{\text{tip}}(z) \propto I_{\text{DC}}$ since the decay lengths (~0.5 Å) of the exchange interaction and the tunnelling current are nearly equal (*25*).

The ESR peaks thus shift with varying tip magnetic field by changing the tip-Ti distance (Fig. S9A). By fitting the total Zeeman energy as a function of tip-Ti distance using equation

(S17) (Fig. S9B), we find a tilting angle θ of ~63.4 degrees for this STM tip (tip #4). Similar measurement performed using tip#3 yields a tilting angle of ~72.7 degrees.

Here B_{tip} is ~40 mT at the tip height where the data of Fig. 3 were measured (V_{DC} = 50 mV, I_{DC} = 3 pA), and $\Delta B_{\mathrm{tip}} = \frac{2\Omega}{\gamma \tan\theta} \approx 1$ mT at V_{RF} = 190 mV. Thus both B_{tip} and ΔB_{tip} are very small compared to the external magnetic field B_{ext} of 0.82 T.

The tip magnetic field can be used to tune the Rabi frequency by changing the tip-Ti distance. As shown in Figs. S9C-D and Fig. 2D, closer tip-Ti distance results in a larger Ω but smaller spin coherence time.

Section 9. Rabi oscillations at detuned RF frequencies

In Fig. S10A, we show the measured Rabi oscillations on a single Ti atom at different detuning frequencies $\Delta\omega = \omega - \omega_0$. In the rotating frame, the Ti spin rotates at the bare Rabi frequency Ω when RF field is in resonance ($\omega = \omega_0$). When detuned away from the Larmor frequency, the spin rotates about a tilted axis $(\Omega, 0, \Delta\omega)$. The oscillation frequency increases as $\Omega^{\mathrm{det}} = \sqrt{\Omega^2 + (\Delta\omega)^2}$, and the oscillation amplitude is reduced (*41, 42*).

The expectation values of the Ti spin $\langle \boldsymbol{S}_{\mathrm{Ti}} \rangle$ in the lab frame is

$$\begin{aligned} \langle S^x_{\mathrm{Ti}} \rangle &= -\frac{1}{2}\left[\sin\xi \sin\Omega^{\mathrm{det}} t \cdot \sin\omega t + \frac{1}{2}\sin 2\xi \left(1 - \cos\Omega^{\mathrm{det}} t\right) \cdot \cos\omega t\right] \\ \langle S^y_{\mathrm{Ti}} \rangle &= \frac{1}{2}\left[\sin\xi \sin\Omega^{\mathrm{det}} t \cdot \cos\omega t - \frac{1}{2}\sin 2\xi \left(1 - \cos\Omega^{\mathrm{det}} t\right) \cdot \sin\omega t\right] \\ \langle S^z_{\mathrm{Ti}} \rangle &= -\frac{1}{4}\left[(1 + \cos 2\xi) + (1 - \cos 2\xi)\cos\Omega^{\mathrm{det}} t\right] \end{aligned} \qquad \text{(S18)}$$

where $\sin\xi = \frac{\Omega}{\sqrt{\Omega^2 + (\Delta\omega)^2}} = \frac{\Omega}{\Omega^{\mathrm{det}}}$.

Following the similar procedure in Section 4, the lock-in signal for the fully coherent case is then:

$$\begin{aligned} V^{\mathrm{det}}_{\mathrm{lock-in}}(\tau) &\propto \mathrm{constant} + \mathrm{K} \cdot \tau \\ &- \sin^2\xi \sqrt{\left(\sin\xi \cdot k_{\mathrm{DC}} - \frac{\cos\xi}{\tan\varphi_{\mathrm{RF}}} \cdot k_{\mathrm{RF}}\right)^2 + k^2_{\mathrm{RF}}} \cdot \sin\left(\Omega^{\mathrm{det}}\tau + \alpha^{\mathrm{det}}\right) \end{aligned} \qquad \text{(S19)}$$

where the constant, the phase shift α^{det} and the linear slope K are all functions of $(V_{\mathrm{RF}}, V_{\mathrm{DC}}, \langle S^x_{\mathrm{t}} \rangle, \langle S^z_{\mathrm{t}} \rangle, \Omega^{\mathrm{det}}, \xi, \varphi_{\mathrm{RF}})$. The linear slope K is also a function of the non-linearity of the *I-V* curve of the Ti atom on MgO.

Thus, the oscillation amplitude is reduced by a factor of ~$\sin^2\xi$.

By adding an additional exponential decay $e^{-\frac{\tau}{T_2}}$, we simulated the Rabi oscillations of a single Ti spin as a function of RF detuning frequency (with zero constant and linear slope K), as shown in Fig. S10C.

Section 10. Spin echo measurement with as a function of τ_2

We performed a spin echo pulse sequence, consisting of a π pulse placed between two π/2 pulses (Fig. S11). The resulting sequence is $\pi/2{-}\tau_1{-}\pi{-}\tau_2{-}\pi/2$, where τ_1 and τ_2 are durations of free precession. When $\tau_1 = \tau_2$, this sequence decouples the spin from any slowly changing magnetic fields (*32*). We implemented this spin echo pulse sequence on the Ti atom. For a fixed

τ_1, we varied τ_2 in order to demonstrate the presence of a spin echo. The Ti spin is refocused to the $|\uparrow\rangle$ state when $\tau_1 = \tau_2$, giving rise to an echo signal.

Section 11. Spin Hamiltonian of Ti dimers

In this section, we describe the spin Hamiltonian of a Ti dimer under applied external magnetic field and the effective magnetic field from the STM tip, which can be written as (*24, 26*):

$$H = \gamma_1\hbar\left(\mathbf{B}_{\text{ext}} + \mathbf{B}_{\text{tip}}\right)\cdot\mathbf{S}_1 + \gamma_2\hbar\mathbf{B}_{\text{ext}}\cdot\mathbf{S}_2 + D_0\left(\mathbf{S}_1\cdot\mathbf{S}_2 - 3(\mathbf{S}_1\cdot\hat{\boldsymbol{r}})(\mathbf{S}_2\cdot\hat{\boldsymbol{r}})\right) + J\,\mathbf{S}_1\cdot\mathbf{S}_2 \quad \text{(S20)}$$

where the first and second terms are the Zeeman energy due to the magnetic field, and the other two terms describe the magnetic coupling within the Ti dimer. $\mathbf{S}_1$ is the spin operator of the Ti atom under the magnetic tip, and γ_1 is its gyromagnetic ratio. $\mathbf{S}_2$ and γ_2 describe the other Ti atom in the dimer on the surface. We use the approximation $\gamma_1 = \gamma_2 = \gamma = 2\mu_{Ti}/\hbar$. The coupling constants $D_0 = \frac{\mu_0\gamma^2\hbar^2}{4\pi r^3}$ and $J = J_0\cdot\exp(-(r - r_0)/d_{\text{ex}})$, where μ_0 is the magnetic constant, d_{ex} is the exponential decay constant of the exchange interaction, and J_0 is the coupling strength at the interatomic distance r_0. The effective tip magnetic field $\mathbf{B}_{\text{tip}} = J_{\text{ts}}\langle\mathbf{S}_{\text{tip}}\rangle/(\gamma\hbar)$. Here, the tip spin is treated classically as a statistical average $\langle\mathbf{S}_{\text{tip}}\rangle$ (*24, 25, 43, 44*), and where the J_{ts} is the coupling constant which is a function of tip-Ti distance.

Hamiltonian (S20) is further simplified to the following form under secular approximation (*45*) (Ti spins are oriented approximately along $\mathbf{B}_{\text{ext}}$ since the Zeeman energy is dominant):

$$\begin{aligned} H &\approx \gamma\hbar S_{1z}\left(B_{\text{ext}} + B_{\text{tip}}\right) + \gamma\hbar S_{2z}B_{\text{ext}} + J\,\boldsymbol{S_1}\cdot\boldsymbol{S_2} + D\,(3S_{1z}S_{2z} - \boldsymbol{S}_1\cdot\boldsymbol{S}_2) \\ &= \gamma\hbar S_{1z}\left(B_{\text{ext}} + B_{\text{tip}}\right) + \gamma\hbar S_{2z}B_{\text{ext}} + (J + 2D)S_{1z}S_{2z} + (J - D)(S_{1x}S_{2x} + S_{1y}S_{2y}) \end{aligned} \quad \text{(S21)}$$

where the direction of $\mathbf{B}_{\text{ext}}$ is defined as direction *z*. The coupling constant $D = \frac{D_0}{2}(1 - 3\cos^2\beta)$ where β is the angle between connecting vector $\hat{\boldsymbol{r}}$ and $\mathbf{B}_{\text{ext}}$. We choose the Zeeman product basis: $|\downarrow\Downarrow\rangle$, $|\downarrow\Uparrow\rangle$, $|\uparrow\Downarrow\rangle$ and $|\uparrow\Uparrow\rangle$, where$|\downarrow\rangle$ and $|\uparrow\rangle$ ($|\Downarrow\rangle$ and $|\Uparrow\rangle$) are the eigenvectors of spin operator S_{1z} (S_{2z}). The eigenstates of Hamiltonian (S21) are

$$\begin{aligned} &|\uparrow\Uparrow\rangle \\ &|+\rangle = \cos\frac{\eta}{2}|\uparrow\Downarrow\rangle + \sin\frac{\eta}{2}|\downarrow\Uparrow\rangle \\ &|-\rangle = \sin\frac{\eta}{2}|\uparrow\Downarrow\rangle - \cos\frac{\eta}{2}|\downarrow\Uparrow\rangle \\ &|\downarrow\Downarrow\rangle \end{aligned} \quad \text{(S22)}$$

where the mixing parameter η is given by $\tan\eta = (J - D)/\gamma\hbar B_{\text{tip}}$.

The eigenenergies of Hamiltonian (S21) are:

$$\begin{aligned} E_{\uparrow\Uparrow} &= \frac{1}{4}(J + 2D) + \frac{1}{2}\gamma\hbar\left(2B + B_{\text{tip}}\right) \\ E_{+} &= -\frac{1}{4}(J + 2D) + \frac{1}{2}\sqrt{(J - D)^2 + (\gamma\hbar B_{\text{tip}})^2} \end{aligned} \quad \text{(S23)}$$

$$E_{-} = -\frac{1}{4}(J + 2D) - \frac{1}{2}\sqrt{(J - D)^2 + (\gamma\hbar B_{\mathrm{tip}})^2}$$

$$E_{\downarrow\Downarrow} = \frac{1}{4}(J + 2D) - \frac{1}{2}\gamma\hbar\left(2B + B_{\mathrm{tip}}\right)$$

When the RF frequency matches the energy difference between the coupled-spin states $|a\rangle$ and $|b\rangle$, the ESR transition will occur if there is a nonzero matrix element: $\langle a|\Delta B_{\mathrm{tip}}^{x} S_{1x}|b\rangle \neq 0$ (S_{1x} is the spin operator of the spin being probed). The Rabi rate $\Omega \propto V_{\mathrm{RF}}\langle a|\Delta B_{\mathrm{tip}}^{x} S_{1x}|b\rangle$.

The four accessible ESR transition frequencies for Ti dimer with antiferromagnetic coupling (Fig. 4E) are defined in order from lowest to highest frequency as:

$$\begin{aligned} f_{\mathrm{I}} &= \frac{1}{\hbar}(E_{-} - E_{\downarrow\Downarrow}) \\ f_{\mathrm{II}} &= \frac{1}{\hbar}(E_{\uparrow\Uparrow} - E_{+}) \\ f_{\mathrm{III}} &= \frac{1}{\hbar}(E_{+} - E_{\downarrow\Downarrow}) \\ f_{\mathrm{IV}} &= \frac{1}{\hbar}(E_{\uparrow\Uparrow} - E_{-}) \end{aligned} \qquad \text{(S24)}$$

The four accessible ESR transition frequencies for the Ti dimer with ferromagnetic coupling (Fig. 4A) are defined in order from lowest to highest frequency as:

$$\begin{aligned} f_{\mathrm{i}} &= \frac{1}{\hbar}(E_{\uparrow\Uparrow} - E_{+}) \\ f_{\mathrm{ii}} &= \frac{1}{\hbar}(E_{-} - E_{\downarrow\Downarrow}) \\ f_{\mathrm{iii}} &= \frac{1}{\hbar}(E_{\uparrow\Uparrow} - E_{-}) \\ f_{\mathrm{iv}} &= \frac{1}{\hbar}(E_{+} - E_{\downarrow\Downarrow}) \end{aligned} \qquad \text{(S25)}$$

The ESR splitting $\Delta f = f_{\mathrm{IV}} - f_{\mathrm{III}} = f_{\mathrm{II}} - f_{\mathrm{I}} = \frac{1}{\hbar}(J + 2D)$ gives the strength of the interaction between two Ti spins on the surface (*24*). For the ferromagnetic case, $\Delta f = f_{\mathrm{iv}} - f_{\mathrm{iii}} = f_{\mathrm{ii}} - f_{\mathrm{i}} = -\frac{1}{\hbar}(J + 2D)$.

The atomically-localized tip field introduces a magnetic asymmetry between the two Ti spins. When the coupling $(J - D)$ is much smaller than Zeeman energy detuning ($\gamma\hbar B_{\mathrm{tip}}$) due to the tip field, as is the case in Fig. 4A, the eigenstates are well described as Zeeman product states (Fig. 4A, right panel). In contrast, when the coupling is larger at closer Ti-Ti distance, the eigenstates are linear superpositions of $|\downarrow\Uparrow\rangle$ and $|\uparrow\Downarrow\rangle$ (Fig. 4E, right panel).

Consider the simple case when the energetic detuning ($\gamma\hbar B_{\mathrm{tip}}$) between $|\downarrow\Uparrow\rangle$ and $|\uparrow\Downarrow\rangle$ is much larger than their coupling $(J - D)$. The eigenstates of the system are then the Zeeman product states, $|\downarrow\Downarrow\rangle$, $|\downarrow\Uparrow\rangle$, $|\uparrow\Downarrow\rangle$ and $|\uparrow\Uparrow\rangle$. Hence, the two allowed transitions are between $|\downarrow\Uparrow\rangle$ and $|\uparrow\Uparrow\rangle$ as well as between $|\downarrow\Downarrow\rangle$ and $|\uparrow\Downarrow\rangle$. These two transitions correspond to peaks iii and iv (*24*).

Each data point in the CW-ESR spectra was averaged over ~10 s. Thus, the measured CW-ESR peak heights reflect the steady-state populations of the four eigenstates. The steady-state

populations of the four energy eigenstates are determined by the Pauli master equations, which contain transition rates between pair of eigenstates due to the scattering with electrons that tunnel between the STM tip and Ag, as well as scattering by Ag substrate electrons (*46*).

Section 12. CW-ESR spectra on a Ti dimer vs tip height

For a Ti spin dimer with fixed coupling, we can also control the state mixing by varying the tip magnetic field at different tip-Ti distance (*24*), since the state mixing is determined by the ratio of the coupling and the tip-field-induced energy detuning. In Fig. S12, we show the CW-ESR spectra of two Ti spin dimers as a function of tip-Ti distance. For the weakly-coupled dimer with a coupling strength ~0.1 GHz (Figs. S12A and B), both detectable ESR peaks show linear frequency shifts with increasing tip magnetic field because the weak state mixing gives states that are approximately Zeeman products states. For the strongly coupled dimer with a coupling strength ~0.9 GHz (Figs. S12C and D), the coupling gives strong mixing of the states. This mixing causes shifting of the peaks that is non-linear in the tip field (the tip field is essentially proportional to I_{DC} for a fixed V_{DC}). For example, the energy difference between the two superposition states can be seen from the frequency difference between peaks I and III. The non-linear frequency shift of these two ESR peaks illustrates that the two superposition states "repel" each other near the avoided level crossing.

Section 13. Pulsed-ESR measurement on Ti dimers at closer distance

We also performed pulsed-ESR measurements on the two Ti dimers at a closer tip-Ti distance (V_{DC} = 50 mV, I_{DC} = 6 pA) than the distance (V_{DC} = 50 mV, I_{DC} = 3 pA) used in Fig. 4. For the Ti dimer with the smaller coupling strength of ~0.1 GHz (Fig. S13A–D), the eigenstates are nearly Zeeman product states at either tip height so only transitions iii and iv are readily detectable (the transitions that simply flip the spin of the atom under the tip). As the tip height is changed, the Rabi frequencies for these transitions remain essentially equal, ($\Omega_{iii} \approx \Omega_{iv}$), as described by the transition matrix element in Section 11 (*24*). In contrast, for the closer dimer with a coupling strength ~0.9 GHz (Fig. S13E–H), transitions I and III are most prominent, and the ratio of their Rabi frequencies Ω_{III}/Ω_{I} becomes larger than the ratio obtained from Figs. 4G and H, indicating less state mixing at larger tip magnetic field.

Section 14. Pulsed-ESR measurement of a single Fe atom

We also performed pulsed-ESR measurement on single Fe atoms on MgO (Fig. S14). The Rabi rate Ω of Fe is smaller by a factor of ~8−10 than that of Ti atoms (we tried three STM tips on Fe). The largest accessible V_{RF} was applied on Fe and yet we were only able to observe ~1−2 Rabi oscillations at most. This is probably due to the nearly vanishing coherent transition rate between the two involved states on Fe, since the main components of these two states differ by spin quantum number $|m_s| = 4$ (*22*). The T_2^{Rabi} times of Fe and Ti are similar (~50 ns) at similar tunneling conditions.

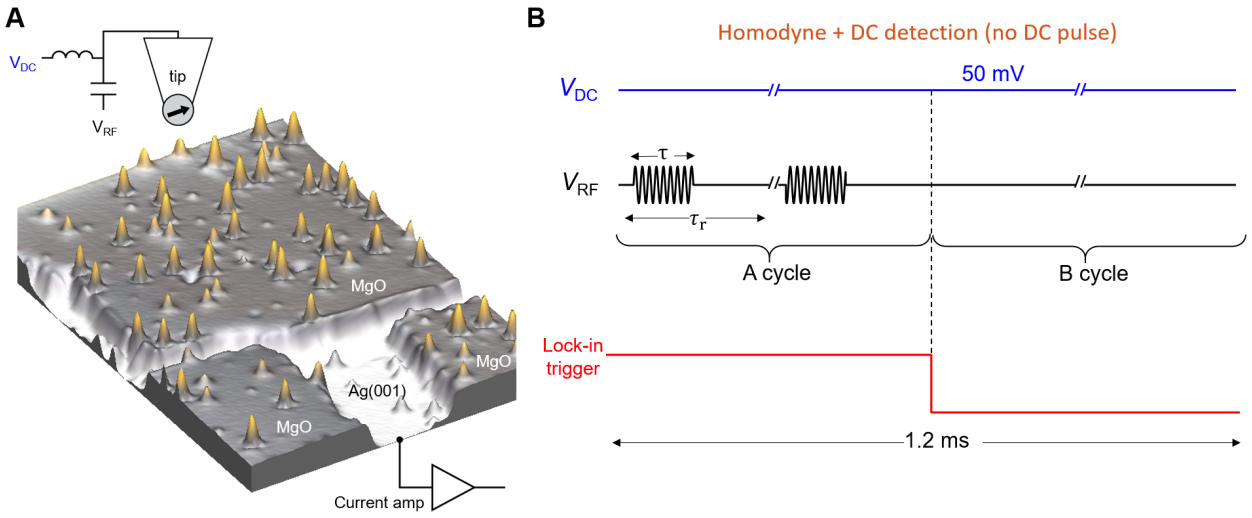

Fig. S1.

(**A**) Large scale STM image (28 nm × 40 nm) of Ti and Fe atoms on MgO/Ag(001) (V_{DC} = 0.1 V, I_{DC} = 10 pA, B_{ext} = 0.90 T, T = 1.2 K). (**B**) Pulse sequences for coherent spin control and detection. A constant V_{DC} (~ 50 mV) is applied in the STM junction. This constant V_{DC} is used to initialize the Ti spin by the spin-polarized current during the time between two RF pulses, and causes decoherence during the coherent manipulations. Both V_{RF} and V_{DC} contribute to the lock-in signals as shown in (S11).

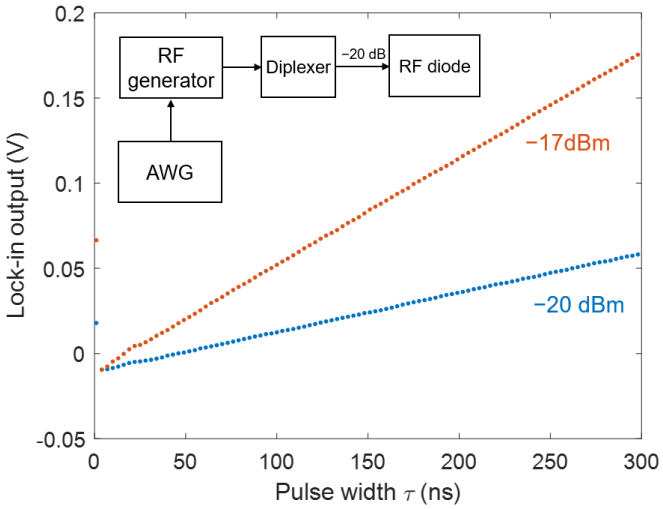

Fig. S2.

Output from the RF diode by a lock-in measurement (818.3Hz) at varying pulse width of the gating voltage (1 V). RF frequency is set to 19 GHz. RF power is −20 dBm (blue points) or −17 dBm (red points). A −20 dB attenuator is added before the RF diode to give −40 dBm or −37 dBm at the diode. Inset shows the measurement diagram.

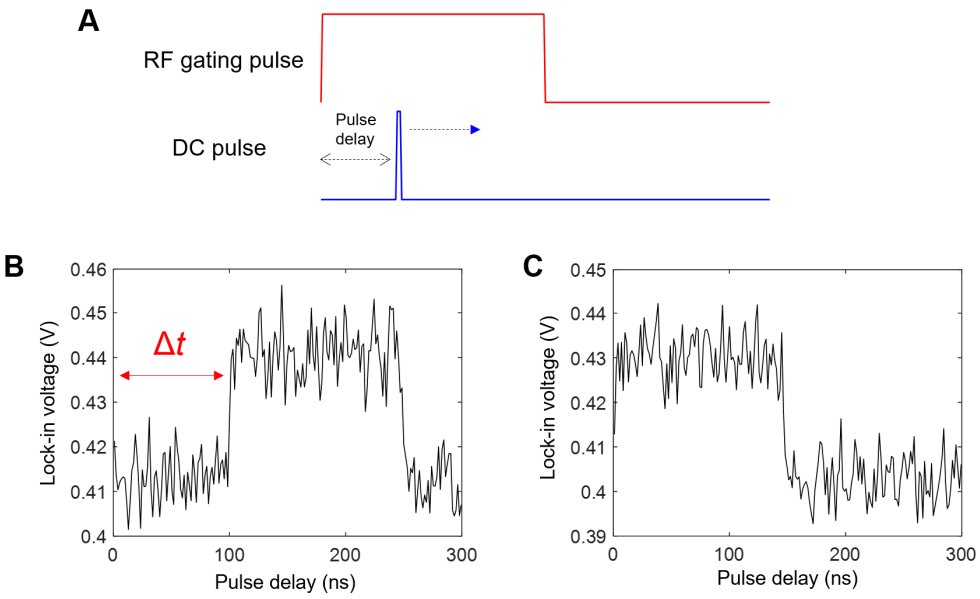

Fig. S3.

(**A**) Schematic showing the scheme for measuring the alignment of the RF and DC pulses. (**B**) The corresponding lock-in output before (left) and after (right) they are aligned (setpoint: V_{DC} = 15 mV, I_{DC} = 200 pA; V_{RF} = 28 mV, f_0 = 22.34 GHz).

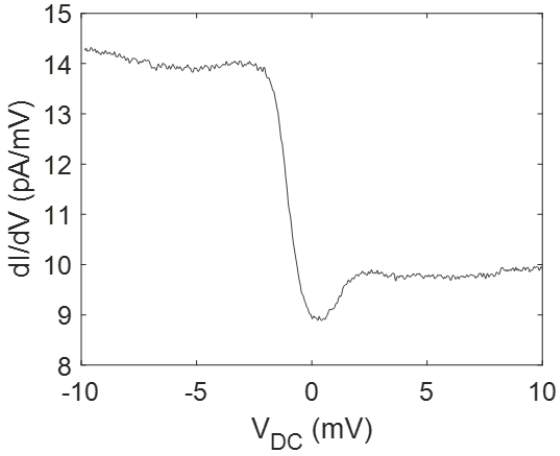

Fig. S4.
dI/dV spectra of Ti on MgO (V_{DC} = 10 mV, I_{DC} = 100 pA, B_{ext} = 0.90 T, T = 1.2 K). Data were taken with tip#1.

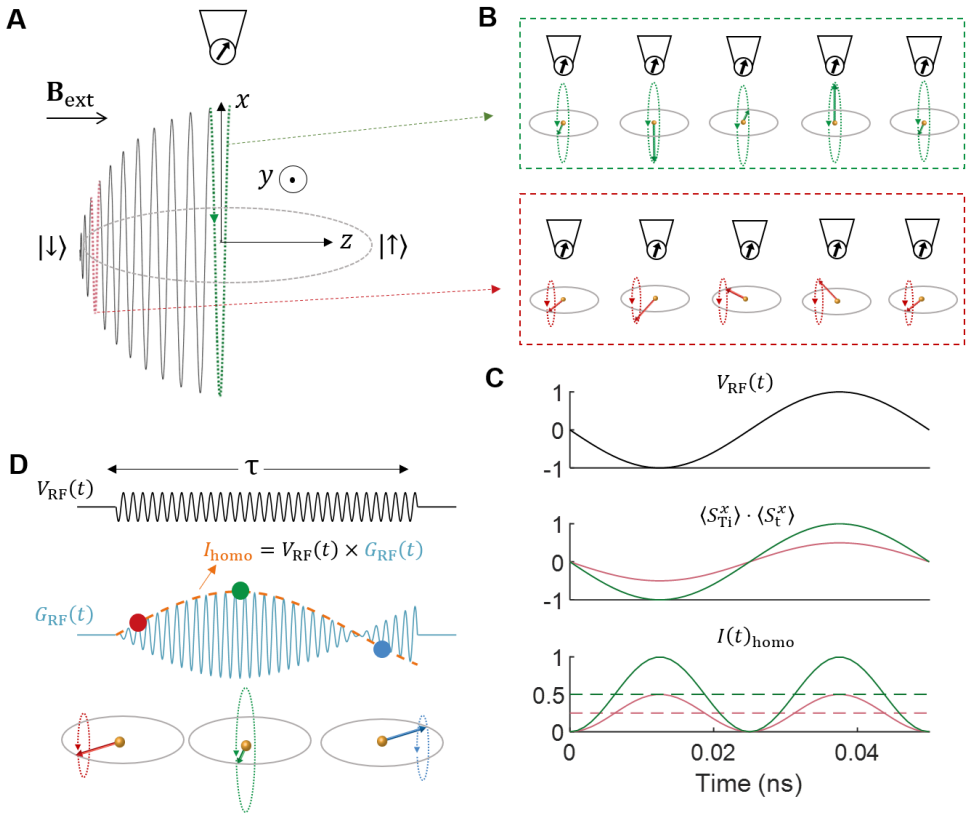

Fig. S5.

Homodyne detection of the Rabi oscillations of a Ti spin. (**A**) Schematic showing the spin rotation in the lab frame, which consists of Larmor precession and the Rabi oscillations. The external field direction is defined as z. The black arrow on the STM tip indicates the orientation of the magnetic moment. (**B**) Snapshots of the Larmor precession for two different Rabi rotation angles. (**C**) Schematic showing the time dependences of RF voltage $V_{\mathrm{RF}}(t)$, the dot product of the x components of the Ti and tip spin which gives rise to the RF conductance $G_{\mathrm{RF}}(t)$, and the homodyne component of the tunneling current $I(t)^{\mathrm{homo}}$. The phase difference between the RF voltage and the precession of the Ti spin in the lab frame φ_{RF} is set to be $\pi/2$. (**D**) The Rabi oscillations are detected by measuring the tunneling current I_{homo}, which is the time average of the product of the RF conductance $G_{\mathrm{RF}}(t)$ and the RF voltage $V_{\mathrm{RF}}(t)$.

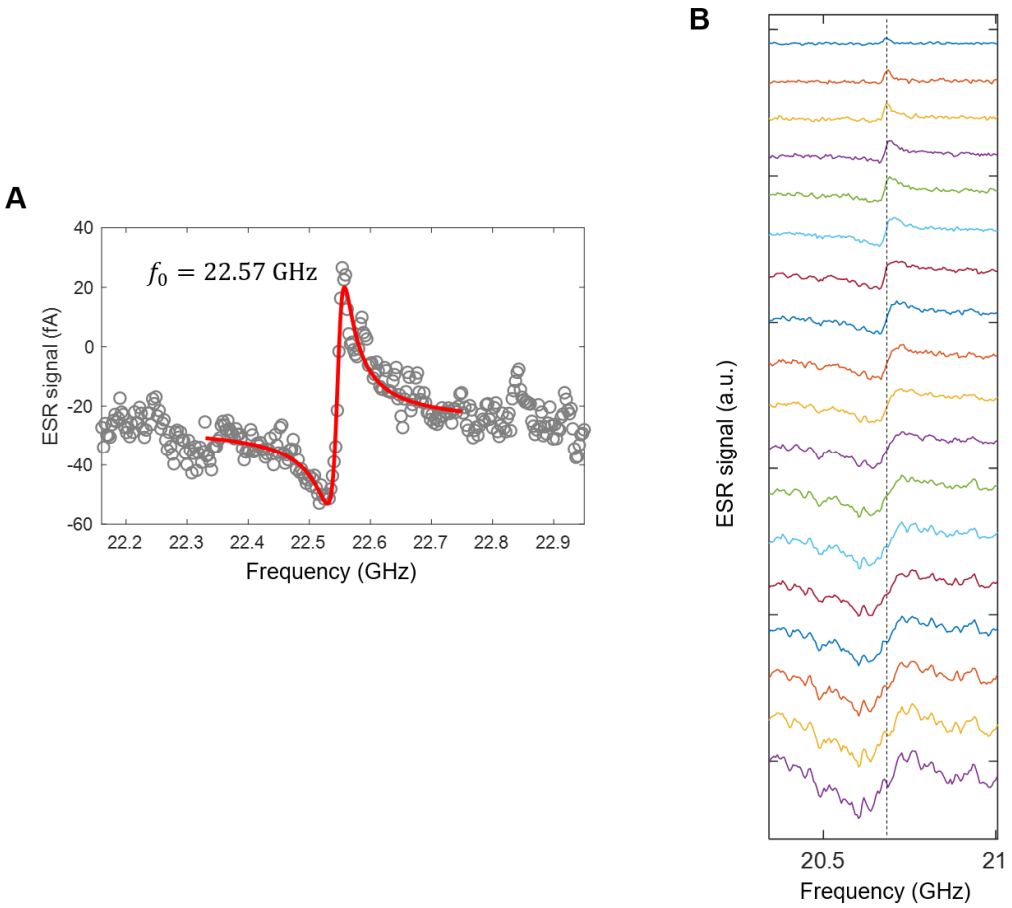

Fig. S6.

(**A**) CW-ESR spectrum of a single Ti atom, fitted to an asymmetric Lorentzian (equation (S14)) (V_{DC} = 60 mV, I_{DC} = 4 pA, V_{RF} = 30 mV, B_{ext} = 0.90 T, T = 1.2 K). Data were taken with tip #1. (**B**) CW-ESR spectra at different RF voltages on a single Ti (setpoint: V_{DC} = 50 mV, I_{DC} = 5 pA, V_{RF} = 10 to 180 mV with increment step of 10 mV; B_{ext} = 0.82 T, T = 1.2 K). ESR spectra were offset for clarity. Data were taken with tip #3.

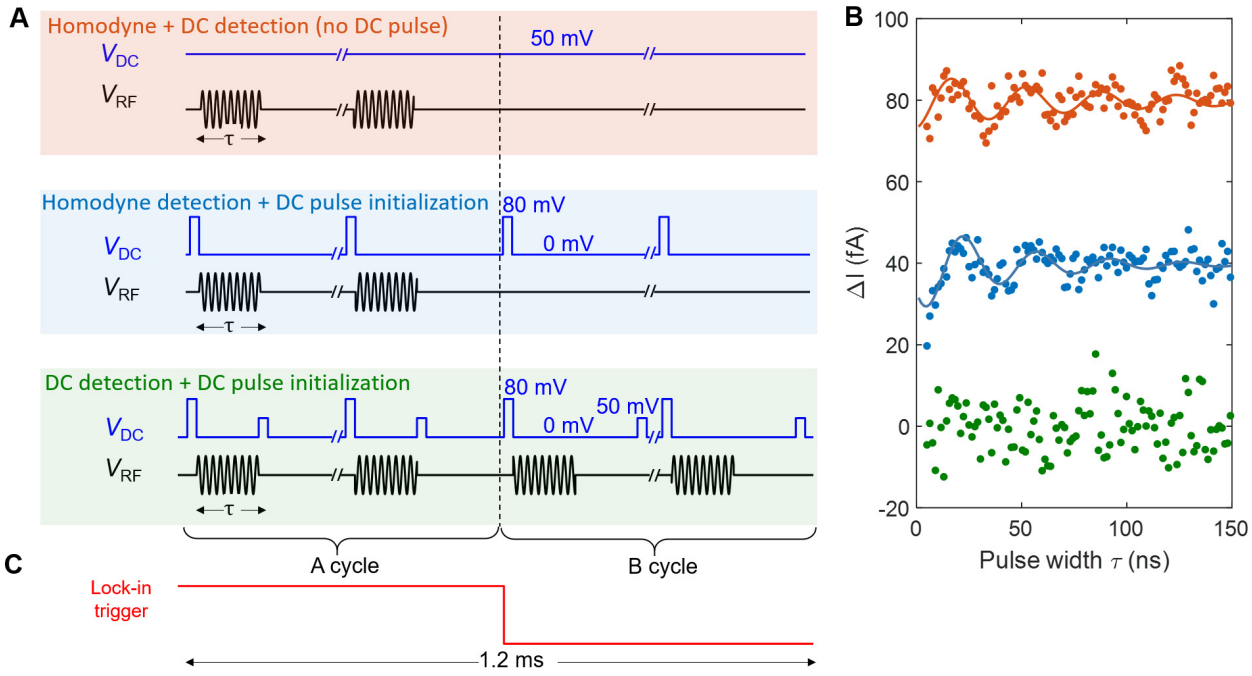

Fig. S7.

(**A**) Different RF and DC pulse schemes used in the experiment. (**B**) Measured Rabi oscillation signals using different pulse sequences. The DC voltages for different schemes are labelled in the figures. (setpoint: V_{DC} = 50 mV, I_{DC} = 5 pA, V_{RF} = 150 mV, B_{ext} = 0.90 T, T = 1.2 K). (**C**) The lock-in trigger voltages for the pulsed-ESR measurements. Data were taken with tip #2.

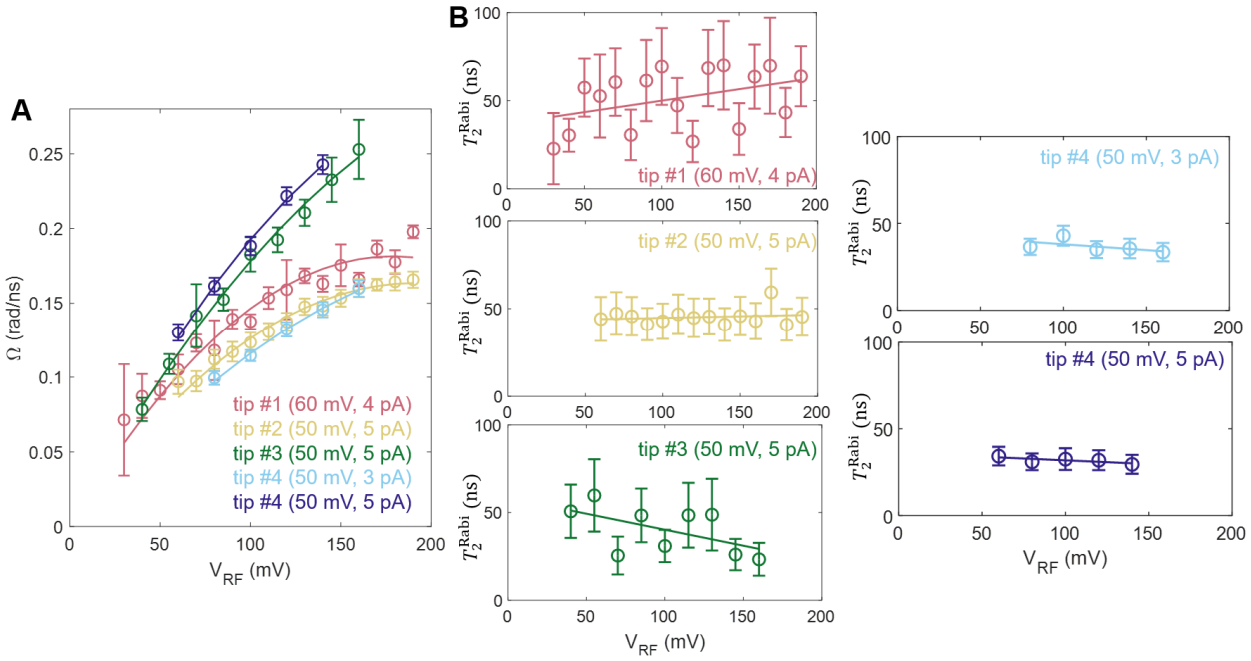

Fig. S8.

Rabi frequency **Ω** (**A**) and spin coherence time T_2^{Rabi} (**B**) as a function of V_{RF} using four different magnetic STM tips, obtained by fitting the Rabi oscillations of a single Ti atom on MgO. The curves in (**A**) are fit to a quadratic polynomial with zero offset. The curves in (**B**) are linear fit, giving T_2^{Rabi} at $V_{\mathrm{RF}} = 0$ of 36.9 ns, 43.0 ns, 58.4 ns, 44.8 ns and 36.0 ns, respectively. The setpoints are labeled in the figures. B_{ext} = 0.90 T for tip #1 and #2, and B_{ext} = 0.82 T for tip #3 and #4.

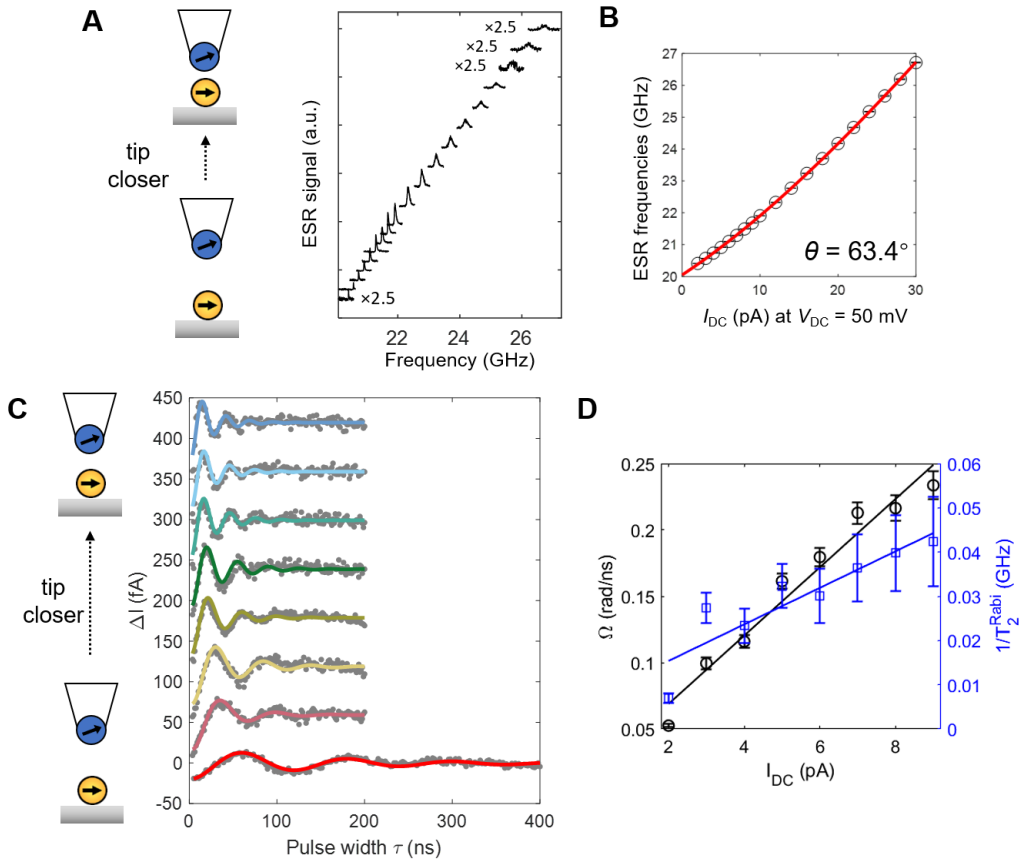

Fig. S9.

(**A**) CW-ESR spectra and (**B**) fitted ESR frequencies at different tip-atom distances set by different I_{DC} at V_{DC} = 50 mV (B_{ext} = 0.82 T, T = 1.2 K). (**C**) Rabi oscillations and (**D**) corresponding Ω and $1/T_2^{Rabi}$ at different tip-atom distances at V_{RF} = 80 mV. Data were taken with tip #4.

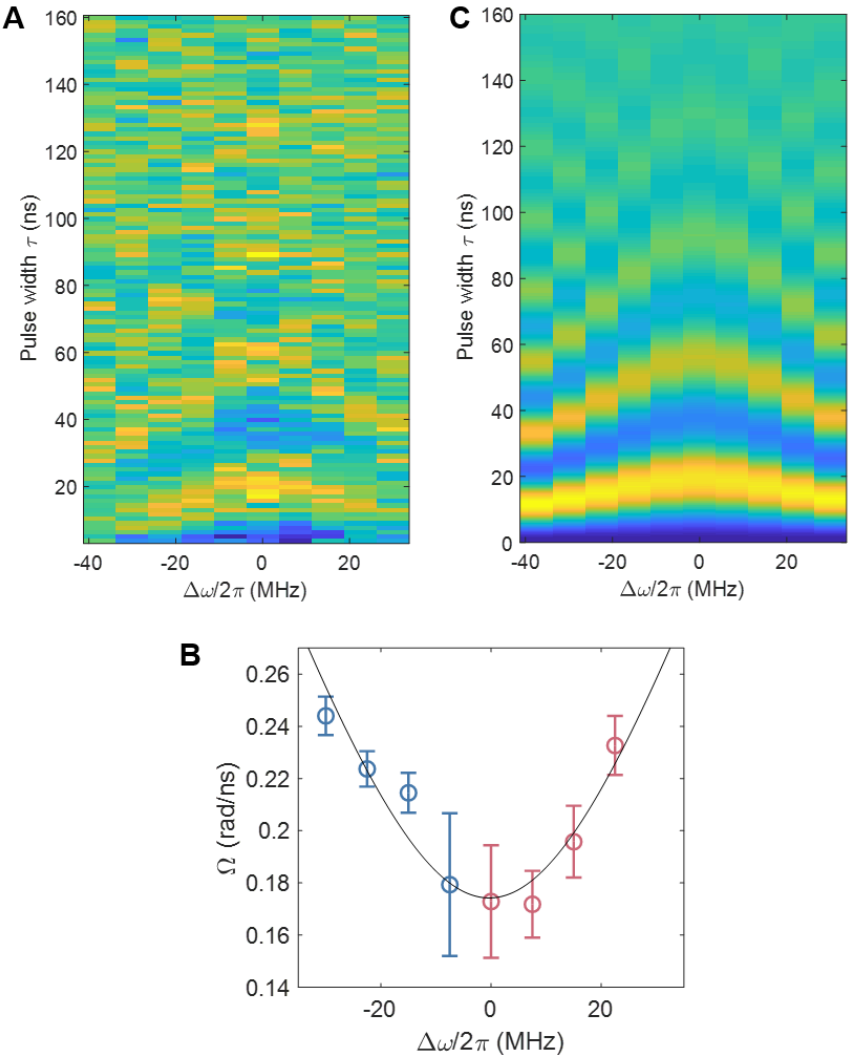

Fig. S10.

(**A**) Rabi oscillations on a single Ti spin as a function of pulse width and RF detuning frequency. The RF detuning from the ESR frequency increases the frequency of the oscillation and decreases the oscillation amplitude (setpoint: V_{DC} = 60 mV, I_{DC} = 4 pA; V_{RF} = 130 mV, f_0 = 22.57 GHz, B_{ext} = 0.90 T). (**B**) Data points are fitted **Ω** from (A) as a function of RF detuning $\Delta\omega$. Black curve is fit to $\sqrt{\Omega^2 + (\Delta\omega)^2}$, giving $\Omega = 0.17 \pm 0.01$ rad/ns. (**C**) The simulated Rabi oscillations on a single Ti spin as a function of pulse width and detuning frequency ($\Omega = 0.17$ rad/ns, $T_2 = 50$ ns). Data were measured with tip #1.

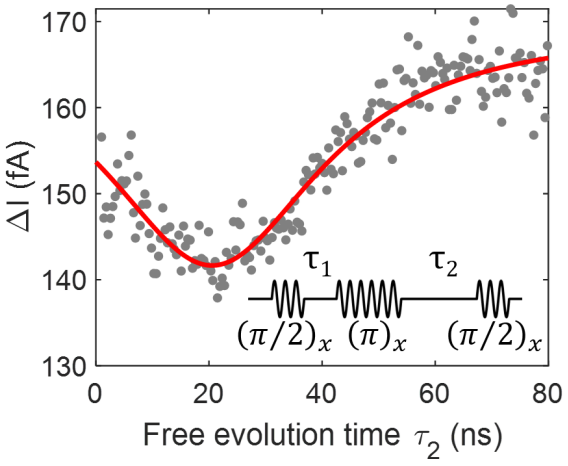

Fig. S11.

Spin-echo signals as a function of τ_2 at τ_1 = 20 ns. RF frequency is in resonance (setpoint: V_{DC} = 50 mV, I_{DC} = 3 pA; V_{RF} = 190 mV, f_0 = 20.54 GHz, B_{ext} = 0.82 T). Red curve is fit to a Gaussian peak. Inset: Pulse scheme for spin echo protocol. Data were measured with tip #4.

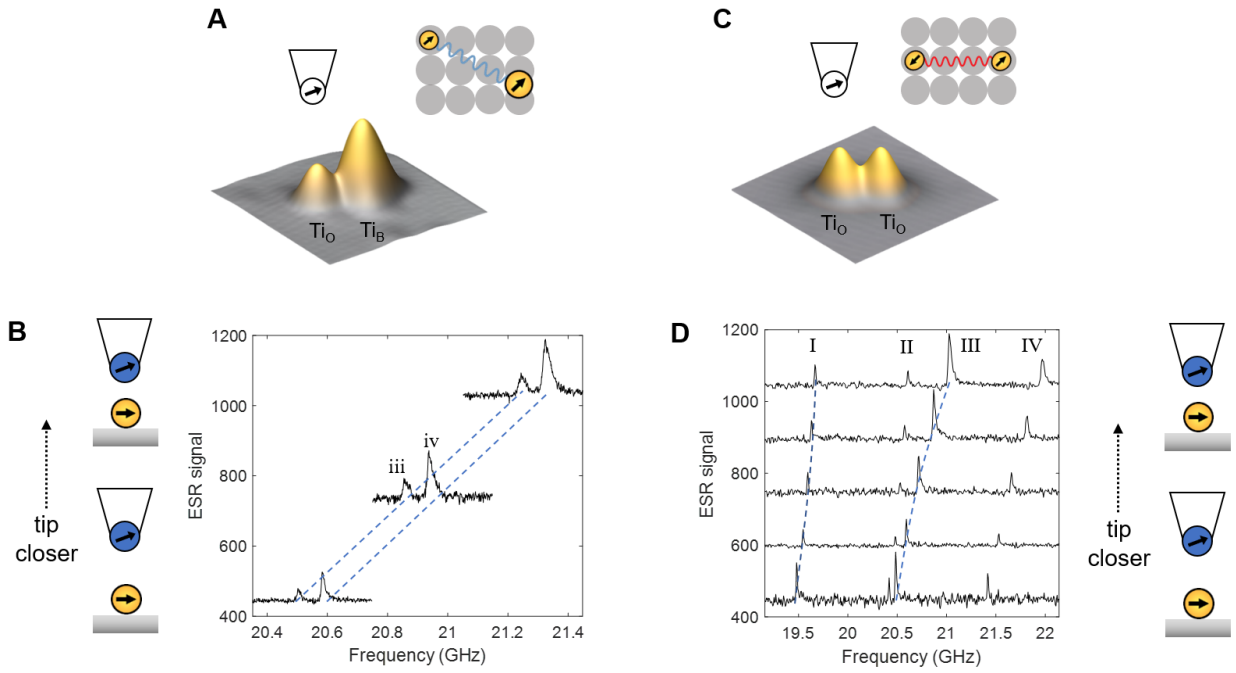

Fig. S12.

(**A**) Schematic of the set-up showing an STM image (4 nm × 4 nm) of two Ti atoms, with one at the oxygen site and the other at a bridge site, and showing the magnetic tip (setpoint: V_{DC} = 60 mV, I_{DC} = 30 pA). (**B**) CW-ESR spectra measured on oxygen-site Ti atom at three different tip fields (setpoint: V_{DC} = 50 mV, I_{DC} = 3, 5 and 7 pA, V_{RF} = 20, 18 and 14 mV, B_{ext} = 0.82 T, T = 1.2 K). Spectra are vertically offset for clarity. The dashed blue lines indicate the positions of the two ESR peaks. (**C**) Schematic of the set-up showing an STM image of two Ti atoms with both at the oxygen site and the magnetic tip (setpoint: V_{DC} = 60 mV, I_{DC} = 30 pA). (**D**) CW-ESR spectra measured on one of the Ti spins at five different tip fields (setpoint: V_{DC} = 50 mV, I_{DC} = 3, 4, 5, 6 and 7 pA, V_{RF} = 25 mV, B_{ext} = 0.82 T, T = 1.2 K). Spectra are vertically offset for clarity in proportion to I_{DC}. The dashed blue lines indicate the positions of the ESR peaks I and III. Data were measured with tip #4.

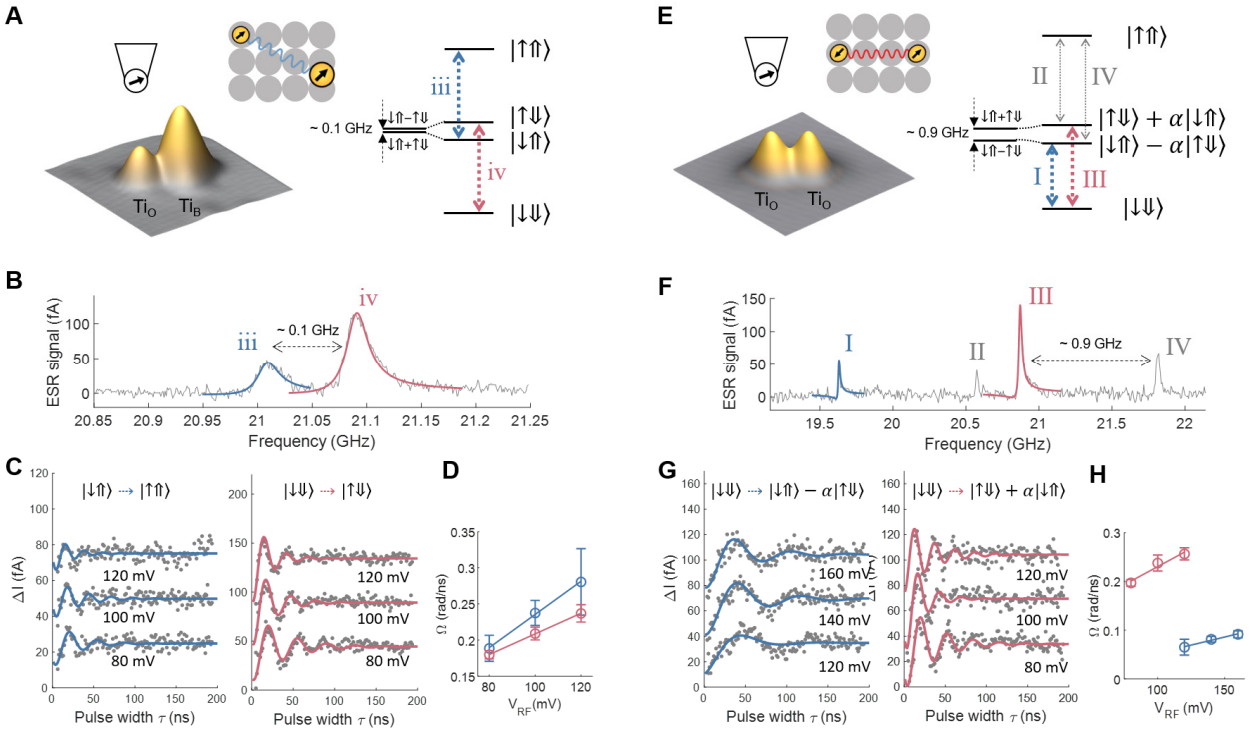

Fig. S13.

Coherent control of spin dimers. (**A**) Left: Schematic showing an STM image (4 nm × 4 nm) of two Ti atoms with one oxygen-site and one bridge-site Ti atom (V_{DC} = 60 mV, I_{DC} = 30 pA), and the magnetic tip. Middle: atom positions of Ti dimers on MgO. Gray circles represent oxygen atoms. Right: energy level diagram with a ferromagnetic coupling of ~0.1 GHz. Dashed arrows indicate ESR transitions. (**B**) CW-ESR measured on the oxygen-site Ti atom (V_{DC} = 50 mV, I_{DC} = 6 pA, V_{RF} =14 mV). (**C**) Pulsed ESR measured on the oxygen-site Ti atom at f = 21.01 GHz and 21.09 GHz, corresponding to the blue and red peaks in (B) (V_{DC} = 50 mV, I_{DC} = 6 pA), showing the coherent transitions from $|\downarrow\Uparrow\rangle$ to $|\uparrow\Uparrow\rangle$ (left), and from $|\downarrow\Downarrow\rangle$ to $|\uparrow\Downarrow\rangle$ (right). (**D**) Dependence of **Ω** on V_{RF} for transitions iii and iv. **Ω** is extracted from a sinusoidal fit in (C). (**E-H**) same as (A−D) except measured on two oxygen-site Ti atoms having a closer spacing, with an anti-ferromagnetic coupling of ~0.9 GHz. (G) shows the coherent transition from $|\downarrow\Downarrow\rangle$ to $|\downarrow\Uparrow\rangle - \alpha|\uparrow\Downarrow\rangle$ (left); and transition III from $|\downarrow\Downarrow\rangle$ to $|\uparrow\Downarrow\rangle + \alpha|\downarrow\Uparrow\rangle$ (right), where $\alpha \approx 0.46$. (H) shows dependence of **Ω** on V_{RF} for transitions I and III. V_{RF} =25 mV in (F). Measured at B_{ext} = 0.82 T, T = 1.2 K. Data were measured with tip #4.

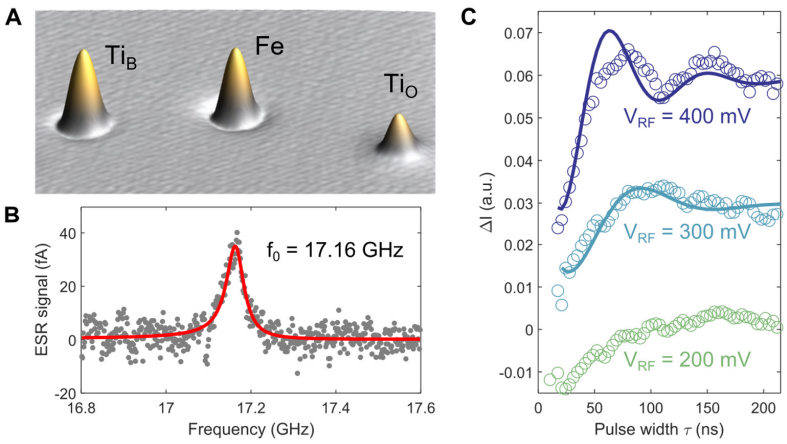

Fig. S14.

(**A**) STM image (12 nm × 12 nm) of Ti and Fe atoms on two layers of MgO on Ag(001) (V_{DC} = 50 mV, I_{DC} = 10 pA). (**B**) CW-ESR spectrum (V_{DC} = 5 mV, I_{DC} = 2 pA, V_{RF} = 10 mV) of the Fe atom shown in panel (A), fitted to an asymmetric Lorentzian (equation (S14)). (**C**) Rabi oscillations of a Fe spin at different V_{RF} as indicated (setpoint as in panel (B)). The RF frequency is on resonance at f_0 = 17.16 GHz obtained from the CW-ESR spectrum. Solid curves are fits to the tunnel current signal ΔI based on the model for damped Rabi oscillations. The data are offset vertically for better visibility. Acquisition time was ~1 hr total for each of the three curves. B_{ext} = 0.90 T, T = 1.2 K.